nature communications

Article

https://doi.org/10.1038/s41467-025-64572-y

FAD synthase confers ferroptosis resistance and restrains CD8$^+$ T cell recruitment in hepatocellular carcinoma

Received: 7 February 2025

Accepted: 17 September 2025

Published online: 29 October 2025

Check for updates

Jiashuo Chao[1,2,3,4,9], Yuan Liang[5,9], Hao Wang[3,9], Ziyu Xun[1,9], Shanshan Wang[6,9], Zhengfeng Xuan[1,9], Mingming Wang[1], Qiyuan Huang[3], Rui Zhang[2], Mu Liu[3], Lei Zhang[3], Bohang Shou[7], Yuhan Zhang[8], Feng Cheng[3,10] ✉, Haitao Zhao[1,10] ✉ & Ling Lu[2,3,10] ✉

Vitamin B2 (VB2) metabolism regulates numerous cellular processes, but its role in hepatocellular carcinoma (HCC) progression remains unclear. Here we show that HCC tumors are characterized by upregulation of a VB2 metabolism signature, and VB2 metabolism promotes HCC progression. Among VB2 metabolic enzymes, flavin adenine dinucleotide synthase (FADS) is the only one that is widely overexpressed in human HCC. Elevated FADS expression correlates with resistance to anti-PD-1 therapy and poor prognosis. In vivo, FADS facilitates HCC cell growth and suppresses T cell-mediated antitumor immunity. Single-cell transcriptomic analysis reveals that FADS-induced changes occur both in the tumor cells and the intra-tumoral CD8$^+$ T cells. Knocking down FADS induces HCC cell death and increases CD8$^+$ T cell infiltration. Mechanistically, FADS confers ferroptosis resistance on HCC cells via enzymatic function to produce FAD and non-enzymatic function to stabilize PCBP2. Moreover, FADS impairs CD8$^+$ T cell recruitment by disrupting the cGAS-STING pathway. Hesperidin, a clinically approved FADS inhibitor, shows antitumor efficacy in a mouse model. Our study thus highlights the importance of VB2 metabolism in HCC and provides the proof of principle for targeting FADS as a therapeutic strategy for HCC.

Hepatocellular carcinoma (HCC) is one of the most prevalent and lethal malignancies worldwide, with over half of cases diagnosed at advanced stages[1]. Despite tyrosine kinase inhibitors, anti-angiogenic therapy, and immune checkpoint inhibitors offer survival benefits for HCC patients, drug resistance frequently occurs, resulting in unsatisfactory clinical outcomes[1]. Therefore, there is an urgent need for improved treatment strategies for HCC.

[1]Department of Liver Surgery, Peking Union Medical College Hospital, Research Unit of Liver Transplantation and Transplant Immunology, Chinese Academy of Medical Sciences and Peking Union Medical College (CAMS & PUMC), Beijing, China. [2]Jiangsu Key Laboratory of Organ Transplantation and Transplant Immunology and Hepatobiliary Center, The Affiliated Hospital of Xuzhou Medical University, Xuzhou, Jiangsu, China. [3]Hepatobiliary Center, The First Affiliated Hospital of Nanjing Medical University, Nanjing, Jiangsu, China. [4]Department of Hepatobiliary and Pancreatic Surgery, Zhejiang Cancer Hospital, Hangzhou Institute of Medicine (HIM), Chinese Academy of Sciences, Hangzhou, Zhejiang, China. [5]School of Biological Science & Medical Engineering, Southeast University, Nanjing, Jiangsu, China. [6]Department of Surgery, Xiang'an Hospital of Xiamen University, School of Medicine, Xiamen University, Xiamen, Fujian, China. [7]Department of Life Science, University of California Los Angeles, Los Angeles, CA, USA. [8]China-Japan Friendship Hospital, Chinese Academy of Medical Sciences and Peking Union Medical College (CAMS & PUMC), Beijing, China. [9]These authors contributed equally: Jiashuo Chao, Yuan Liang, Hao Wang, Ziyu Xun, Shanshan Wang, Zhengfeng Xuan. [12]These authors jointly supervised this work: Feng Cheng, Haitao Zhao, Ling Lu.
✉e-mail: docchengfeng@njmu.edu.cn; zhaoht@pumch.cn; lvling@njmu.edu.cn

Metabolic reprogramming is a cancer hallmark. Tumor cells rewire metabolic pathways to fulfill energy and biosynthesis, survive in the harsh microenvironment, and evade immune surveillance[2]. Understanding how dysregulated metabolism contributes to tumor progression offers mechanistic insights and identifies actionable metabolic vulnerabilities. Most studies focus on the dysregulation of major metabolic pathways such as glucose, lipid, and amino acid metabolism. Recently, vitamins metabolism in tumor progression and treatment resistance attracts attention[3–5]. For instance, vitamin B5 accumulated in MYC-overexpressing mammary tumors, where its conversion to coenzyme A fuels the tricarboxylic acid cycle, promoting tumor growth[3]. Vitamin B3 has been shown to inhibit the immunosuppressive polarization of myeloid cells and enhance antitumor immunity in liver cancer[4]. In addition, vitamin E promotes tumor antigen cross-presentation by dendritic cells, thereby increasing the efficacy of cancer immunotherapies[5]. Despite these findings, the role of vitamin metabolism in cancer remains underexplored.

Vitamin B2 (VB2), namely riboflavin, is an essential micronutrient for human health. It cannot be synthesized endogenously and must be obtained by dietary intake[6]. After cellular uptake, VB2 is rapidly converted into its active forms, flavin mononucleotide (FMN) and flavin adenine dinucleotide (FAD), as VB2 itself is not directly usable[7]. FMN and FAD are well-known as coenzymes for flavoproteins, which catalyze numerous redox reactions critical for cellular processes[8]. The conversion of VB2 to FMN and FAD requires two key enzymes, riboflavin kinase (RFK, encoded by *RFK*) and FAD synthase (FADS, encoded by *FLAD1*)[9]. Hu et al. reported that FADS expression is upregulated in gastric cancer, and its high expression is correlated with poor prognosis[10]. Recent findings suggested that FADS may be associated with malignancy and stemness in pancreatic ductal adenocarcinoma cells[11]. However, experimental investigations into the role of FADS in cancer are still limited. Barile and colleagues highlighted the multifaceted roles of flavins and flavoproteins, noting that RFK and FADS are poorly investigated in cancer[9].

VB2 is absorbed in the small intestine, then released into the portal vein and transported to the liver[6]. A previous study found that plasma VB2 levels were lower in early-stage HCC patients than in healthy individuals, and even lower in those with advanced-stage disease[12]. In addition, elevated serum levels of riboflavin transporters were reported in HCC patients compared to healthy and cirrhotic controls[13]. These findings showed the relationship between VB2 metabolism and HCC, but whether and how VB2 metabolism affects HCC progression remains elusive.

Here, we show that VB2 metabolism is activated in HCC tumors and facilitates disease progression. Among its metabolic enzymes, FADS, rather than RFK, is widely overexpressed in human HCC. Functionally, FADS not only confers ferroptosis resistance on HCC cells to support tumor growth, but also impedes $CD8^+$ T cell recruitment to dampen antitumor immunity. Inhibiting FADS causes notable tumor regression in vivo. Our study reveals FADS as an actionable metabolic target in HCC and highlights its therapeutic potential.

Results

HCC cells exhibit the activation of VB2 metabolism

As the activation levels of metabolic pathways can be quantified by integrating the expression levels of pathway-related genes, we defined a VB2 metabolism gene signature (*SLC52A1*, *SLC52A2*, *SLC52A3*, *RFK*, *FLAD1*, *ACP5*, and *ENPP1*) based on the Reactome pathway database, and then calculated a VB2 metabolism score by integrating the gene signature. Analysis of three HCC datasets (TCGA-LIHC, OPE000321, and ICGC-LIRI-JP) revealed significantly higher VB2 metabolism scores in tumors compared to adjacent liver tissues (Fig. 1a), suggesting that VB2 metabolism is hyperactive in HCC. Notably, patients with higher VB2 metabolism scores exhibited poorer prognoses (Fig. 1b).

The complexity of the tumor microenvironment (TME) suggests that activation of VB2 metabolism may differ across various cell types. To assess VB2 metabolism levels within distinct cell populations in the TME, we performed single-cell RNA-seq (scRNA-seq) on HCC biopsy samples from our Immunotherapy Cohort ($n = 8$, details in Supplementary Data. 1). A total of 81,250 cells was identified and classified into seven major cell types (Fig. 1c, d). Epithelial cells were further classified into 18,642 tumor cells and 5239 normal cells using the InferCNV algorithm. Results showed that tumor cells possessed the highest VB2 metabolism scores among all identified cell types, and significantly higher than normal epithelial cells (Fig. 1e). This finding was validated using an external scRNA-seq dataset (GSE202642), which also demonstrated higher VB2 metabolism scores in tumor cells compared to normal epithelial cells (Fig. 1f, g and Supplementary Fig. 1)[14]. Collectively, both internal and external datasets consistently indicate that tumor cells have relatively elevated VB2 metabolism. We subsequently focused our analysis on tumor cells.

VB2 metabolism facilitates the malignant behaviors of HCC cells

The effects of VB2 metabolism on HCC cells were investigated in terms of metabolites and enzymes (Fig. 1h). Treatment of Hep3B and HCCLM3 cells with VB2, FMN, or FAD led to increased cell viability and migration (Fig. 1i and Supplementary Fig. 2a). In contrast, treatment with lumiflavin, a riboflavin inhibitor, reduced HCC cell viability (Supplementary Fig. 2b). To further assess the in vivo effects, subcutaneous tumors were established with murine Hepa1-6 cells in *Rag1*$^{-/-}$ mice (immune-deficient, lack of T and B cells). Intratumoral injection of VB2, FMN, or FAD accelerated tumor growth and increased tumor weight (Fig. 1j and Supplementary Fig. 2c).

We next investigated the role of VB2 metabolic enzymes in HCC cells. Lentiviral-mediated shRNA knockdown (sh*RFK*, sh*FLAD1*) and plasmid-based overexpression (*RFK*-OE, *FLAD1*-OE) of RFK and FADS were performed in Hep3B and HCCLM3 cells (Supplementary Fig. 3a, b). Knockdown of RFK or FADS significantly inhibited cell proliferation and colony formation (Fig. 1k), while overexpression promoted cell proliferation (Supplementary Fig. 3c). Consistently, knockdown of Fads in murine Hepa1-6 cells (sh*Flad1*) also decreased proliferation and colony formation (Supplementary Fig. 3d). Furthermore, knockdown of RFK or FADS inhibited cell migration and invasion (Fig. 1l and Supplementary Fig. 3e), while overexpression of RFK or FADS enhanced migration (Supplementary Fig. 3f).

Collectively, these results demonstrate that VB2 metabolism plays a crucial role in supporting the malignant behaviors of HCC cells.

FADS, rather than RFK, is widely overexpressed in human HCC

The activation of VB2 metabolism depends on RFK and FADS, as VB2 must be converted into FMN and FAD to be utilized by cells. However, the expression patterns of RFK and FADS in human HCC remain unclear.

To address this, we first analyzed 18 HCC datasets, comprising 2537 tumors and 1821 non-tumor liver samples (Supplementary Data. 2). *FLAD1* expression was significantly upregulated in tumors in 17 out of 18 datasets (Fig. 2a), whereas *RFK* expression was comparable between tumors and livers in half of the datasets (Supplementary Fig. 4a). Second, analysis of surgical samples from our Cohort-A ($n = 30$; Supplementary Data. 1) showed that *FLAD1* mRNA was higher in most tumors compared to paired liver tissue (Fig. 2b), while *RFK* mRNA levels were comparable in most patients (Supplementary Fig. 4b). At the protein level, FADS was markedly upregulated in tumors compared to paired liver tissues (Fig. 2c), while RFK showed no tendency of differential expression (Supplementary Fig. 4c). Third, we constructed a tissue microarray using samples from Cohort-B ($n = 42$; Supplementary Data. 1). Immunohistochemical (IHC) analysis revealed higher H-scores of FADS in tumors compared to non-tumor livers

https://doi.org/10.1038/s41467-025-64572-y

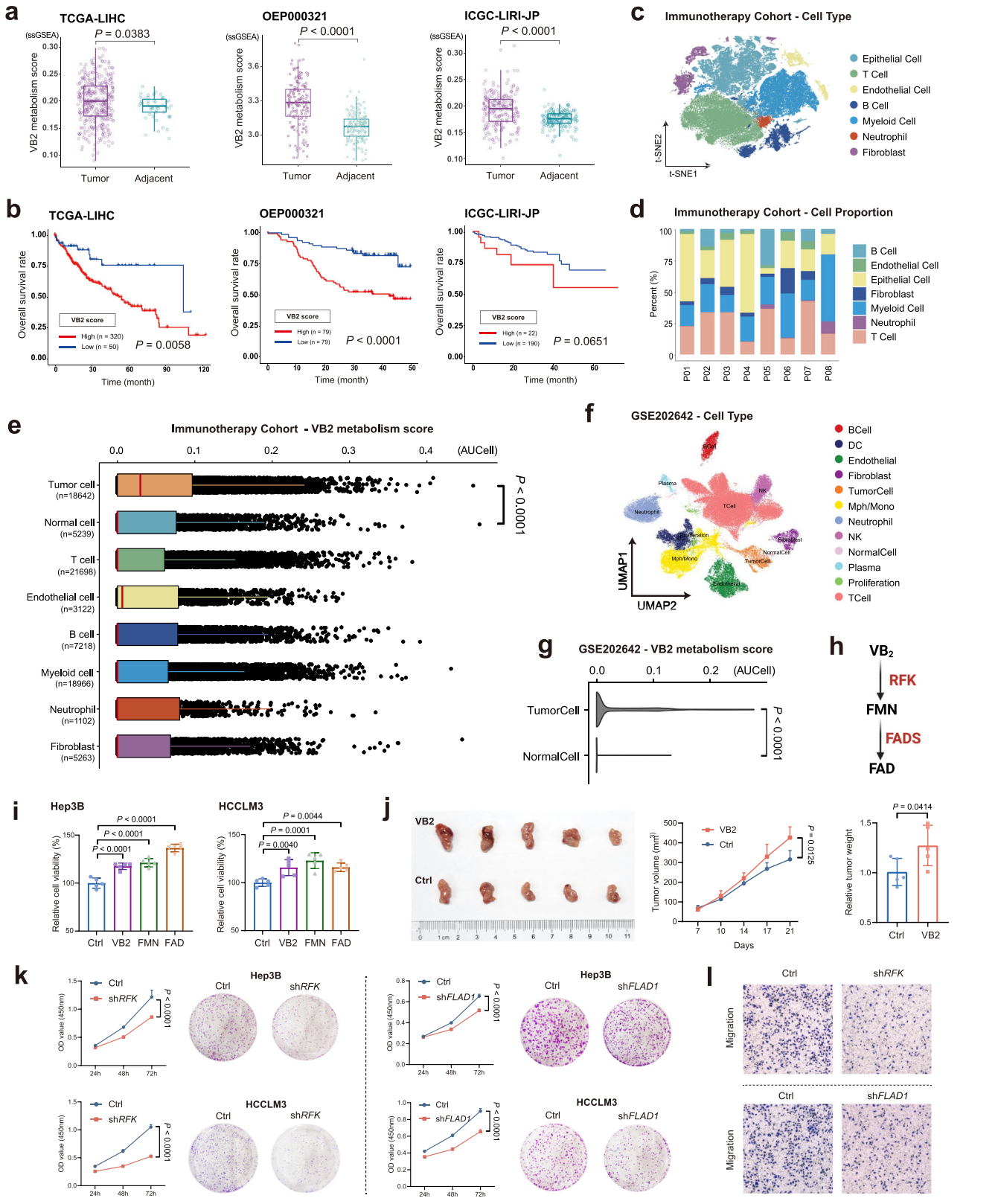

(Fig. 2d), whereas H-scores of RFK were comparable between tumors and livers (Supplementary Fig. 4d).

Fourth, in human hepatocytes (THLE-2) and five HCC cell lines (Huh7, Hep3B, HCCLM3, MHCC97H, and MHCC97L), FADS expression was consistently higher in all HCC cell lines than in hepatocytes, whereas RFK was upregulated in only three of the five HCC lines (Supplementary Fig. 5a). Notably, knockdown of RFK in THLE-2 cells inhibited proliferation, while FADS knockdown had no effect on hepatocyte proliferation (Supplementary Fig. 5b), suggesting that FADS may have a tumor-specific role.

Collectively, these findings demonstrate that FADS, but not RFK, is consistently overexpressed in human HCC.

Fig. 1 | VB2 metabolism promotes HCC progression. a Comparisons of VB2 metabolism scores between tumors and non-tumor livers from TCGA-LIHC, OEP000321, and ICGC-LIRI-JP datasets. Scores were calculated for each sample using the ssGSEA algorithm based on a VB2 metabolism gene signature. **b** Kaplan-Meier overall survival curves stratified by VB2 metabolism scores, with optimal cutoffs determined by the surv_cutpoint function. **c** t-SNE visualization showing 7 major cell types in tumor samples from the immunotherapy cohort ($n = 8$). **d** Proportions of the 7 major cell types across the eight patients. **e** Box plots with medians (red line) and interquartile ranges depicting VB2 metabolism scores in various cell types. Scores were calculated with the AUCell algorithm based on the VB2 metabolism gene signature. **f** UMAP plot showing 12 major cell types in the GSE202642 dataset. **g** Violin plot showing VB2 metabolism scores among tumor cells and normal epithelial cells in GSE202642. **h** Schematic diagram of the VB2 metabolic pathway with metabolites in black and enzymes in red. **i** Hep3B and HCCLM3 cells treated with VB2 (10 μM), FMN (10 μM), FAD (10 μM), or PBS (Ctrl) for 48 h, followed by CCK-8 assay ($n = 5$ biological replicates). **j** Subcutaneous tumors were established in *Rag1*$^{-/-}$ mice with Hepa1-6 cells ($n = 5$ per group). Mice received daily intratumoral injections of VB2 (50 mg/kg) or control solvent from day 5 to day 21. Tumor volumes were measured at the indicated timepoints. Tumors were photographed and weighed at day 21. **k** Proliferation of Hep3B and HCCLM3 cells with lentiviral knockdown of RFK (sh*RFK*) or FADS (sh*FLAD1*) ($n = 5$ biological replicates), as determined by CCK-8 assay and colony formation assay. **l** Migration of HCCLM3 cells with RFK or FADS knockdown, assessed by transwell assay ($n = 3$ biological replicates). For bar graphs, data are presented as mean ± SD (**i**–**k**). For box plots (**a**, **e**), the box shows the median with interquartile ranges (IQR), whiskers extend to 1.5 × IQR, and outliers are shown as individual points. *P*-values were calculated using one-way ANOVA with Tukey's test (**i**, **k**), two-way ANOVA with Tukey's test (**j**, **k**), unpaired two-sided Student's *t* test (**j**), two-sided Wilcoxon rank-sum test (**a**, **e**, **g**), and log-rank test (**b**). Source data are provided as a Source Data file.

Elevated FADS expression corelates with anti-PD-1 resistance and unfavorable prognosis

In TCGA-LIHC and OPE000321 cohorts, patients with higher *FLAD1* expression showed worse overall survival (Fig. 2e). As immunotherapy is an effective option for unresectable HCC, we investigated whether *FLAD1* expression correlates with immunotherapy response. In Fudan Cohort (17 HCC patients receiving anti-PD-1 therapy)[15], patients with progressive disease exhibited significantly higher *FLAD1* expression than those with partial response ($P = 0.0388$, Fig. 2f). Furthermore, higher *FLAD1* expression was associated with inferior response to anti-PD-1 therapy ($P = 0.0498$, Supplementary Fig. 6a). In our Immunotherapy Cohort ($n = 8$), all patients received anti-PD-1 therapy, and treatment responses were evaluated using mRECIST (modified Response Evaluation Criteria in Solid Tumors) criteria. Of these, 4 patients achieved partial response and 4 had stable disease (Supplementary Fig. 6b). ScRNA-seq analysis revealed that patients with stable disease harbored a higher proportion of *FLAD1*+ tumor cells compared to those with partial response, although this difference did not reach statistical significance ($P = 0.11$, Fig. 2g).

Collectively, these findings suggest that high *FLAD1* expression is associated with resistance to anti-PD-1 therapy and poorer prognosis in HCC patients.

FADS promotes HCC cell growth and restrains T cell-mediated antitumor immunity

To investigate the role of FADS in HCC progression, we established tumor models in immune-competent C57BL/6 mice using Hepa1-6 cells with Fads knockdown (sh*Flad1*) or control cells (Ctrl). In subcutaneous models, Fads knockdown significantly inhibited tumor growth and reduced tumor weight (Fig. 2h). Notably, Fads-knockdown tumors grew during the first 10 days but subsequently began to shrink and regress, while control tumors continued to grow. Fads-knockdown tumors appeared pale, less elastic, and had a hardened texture, indicative of tumor necrosis. In orthotopic models, Fads knockdown significantly inhibited tumor growth and reduced the weight of tumor-bearing liver (Fig. 2i). Similar to subcutaneous tumors, orthotopic Fads-knockdown tumors shrank between days 14 and 21, whereas control tumors maintained growth (Fig. 2j).

The observed tumor regression after Fads knockdown could not be solely attributed to impaired HCC cell proliferation, suggesting involvement of additional mechanisms. Based on the predator-prey theory of tumor immunity[16], tumor regression may result from increased vulnerability of tumor cells and enhanced antitumor immunity. Given the pivotal role of T cells, particularly CD8$^+$ T cells, in antitumor immunity, we hypothesized that T cells may contribute to the tumor regression.

To test this, we generated tumor models in *Rag1*$^{-/-}$ mice (lack of T and B cells). In subcutaneous models, Fads knockdown still inhibited tumor growth and reduced tumor weight, but the difference was not as remarkable as in C57BL/6 mice (Fig. 2k), and the tumors did not regress but continued growing. In orthotopic models, a similar trend was observed that Fads knockdown reduced tumor burden, but the difference was not as pronounced as in C57BL/6 mice (Fig. 2l). Moreover, Fads-knockdown tumors grew continuously, distinct from the tumor regression observed in C57BL/6 mice (Fig. 2m). These findings confirm the importance of T cells in mediating tumor regression. However, T cells alone could not eliminate control tumors, whereas loss of FADS rendered tumor cells susceptible to T cell clearance, indicating that loss of FADS amplifies T cell-mediated antitumor immunity. In addition, delayed tumor growth of Fads-knockdown cells in both immune-deficient and immune-competent mice suggests a direct inhibitory effect of FADS loss on HCC cell growth in vivo.

Given the prevalence of macrophages in tumors, we also examined their role in FADS knockdown-mediated tumor regression using macrophage depletion experiments by administration of Clodronate-liposomes (Supplementary Fig. 7a, b). In mice treated with clodronate liposomes, control tumors continued to grow, while Fads-knockdown tumors underwent early regression, with the Fads-knockdown tumors showing significantly reduced tumor volume and weight compared to control tumors (Supplementary Fig. 7c–e). It was consistent with the results observed in mice treated with PBS-liposome (Supplementary Fig. 7c–e). In addition, in mice inoculated with Ctrl cells, clodronate-liposome treatment significantly suppressed tumor growth and reduced tumor weight compared to PBS-liposome controls (Supplementary Fig. 7c–e), suggesting that macrophages promoted tumor progression. Thus, macrophages were not involved in FADS knockdown–induced tumor regression.

Overall, our findings demonstrate that FADS promotes HCC progression by supporting tumor cell growth and suppressing T cell-mediated antitumor immunity.

Single-cell transcriptomic analysis reveals the impact of FADS on tumor microenvironment

To comprehensively delineate the impact of FADS on the TME, especially tumor cells and T cells, we established orthotopic tumors in C57BL/6 mice using Hepa1-6 cells. Tumors were harvested at day 14 for scRNA-seq (Fig. 3a). In total, 10 samples (5 FADS-knockdown tumors [KD] and 5 control tumors [NC]) yielded 128,884 cells for downstream analysis (Fig. 3b). Unsupervised clustering identified 29 distinct cell clusters (Supplementary Fig. 8a), which were categorized into 15 major cell types (Fig. 3b and Supplementary Fig. 8b). To distinguish malignant tumor cells from normal epithelial cells, we applied a normal hepatocyte gene signature (Supplementary Fig. 8c and Supplementary Data. 3)[17].

We first focused our analysis on tumor cells. scDist analysis revealed that tumor cells exhibited the most significant perturbations after FADS knockdown (Fig. 3c). Tumor cells in Fads-knockdown

https://doi.org/10.1038/s41467-025-64572-y

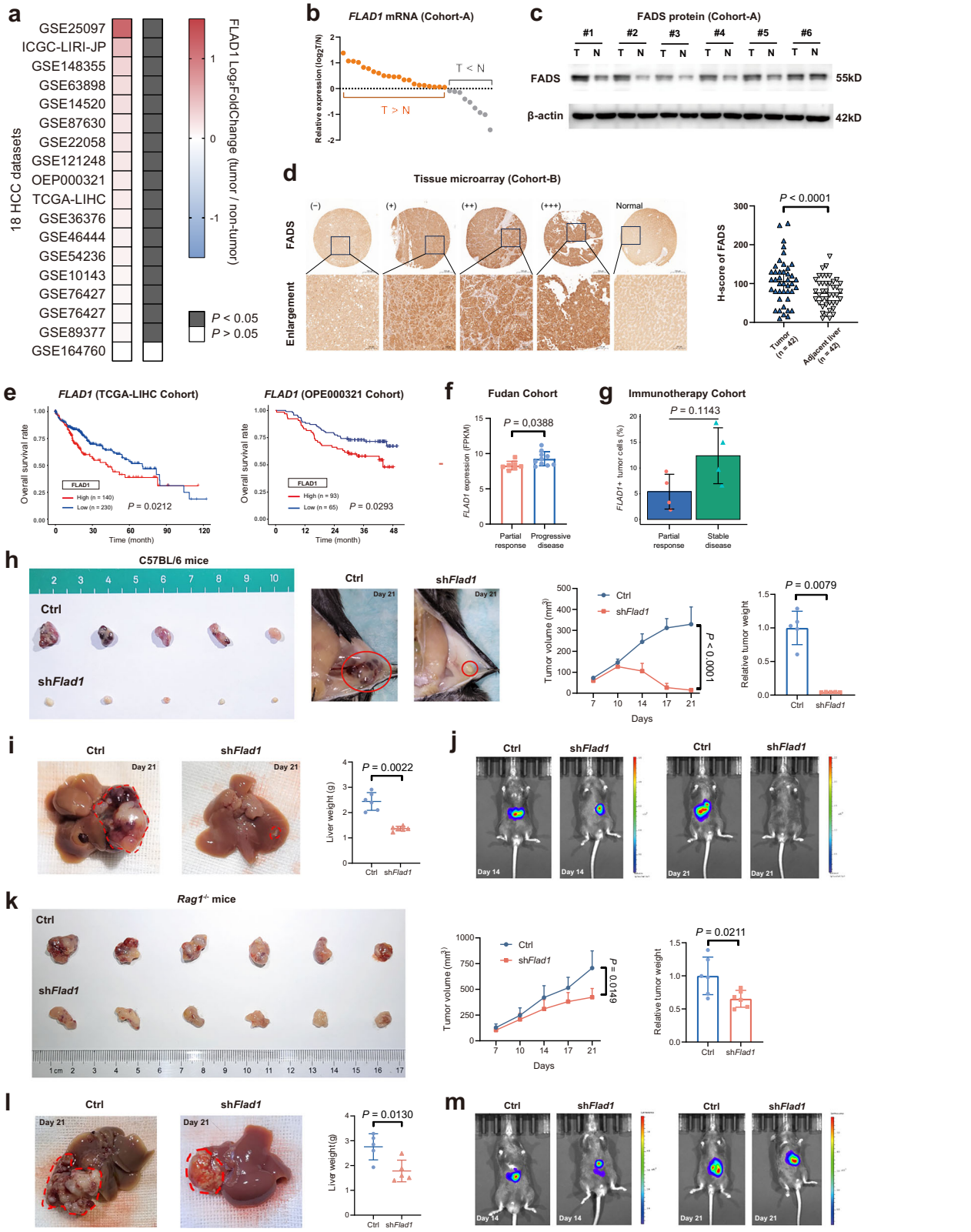

tumors showed lower *Flad1* expression and lower VB2 metabolism score compared to those in control tumors (Fig. 3d and Supplementary Fig. 8d), suggesting that loss of FADS impairs VB2 metabolism activity. KEGG enrichment analysis of tumor cells identified significant alterations in metabolic pathways, including glucose, lipid, and amino acid metabolism, as well as immune-related pathways such as chemokine and cytokine signaling (Fig. 3e and Supplementary Fig. 8e). Notably, pathways related to cell death, including ferroptosis and apoptosis, were also enriched (Fig. 3e).

Given our in vivo findings, we next turned our attention to T cells. T & NK lymphocytes were re-clustered into 16 subsets, including 7 distinct $CD8^+$ T cell populations (Fig. 3f and Supplementary Fig. 9a, b). T cell subsets were further annotated by canonical T cell signature (Supplementary Fig. 9c)[18]. Six out of seven $CD8^+$ T cell subsets (C11,

Fig. 2 | FADS promotes tumor growth and restrains T cell-mediated antitumor immunity. a Comparison of *FLAD1* expression between tumors and non-tumor liver samples in 18 HCC datasets from the HCCDB database. **b** *FLAD1* mRNA levels in paired tumors (T) and adjacent livers (N) from Cohort-A ($n = 30$ pairs). **c** FADS protein levels in paired tumors (T) and adjacent livers (N) from Cohort-A ($n = 6$ pairs). Data from 3 independent experiments with similar results. **d** Representative images and quantification of FADS staining in paired tumors and liver samples from Cohort-B ($n = 42$ pairs). Quantification is based on H-scores. **e** Kaplan-Meier overall survival curves of TCGA-LIHC and OEP000321 cohorts, stratified by *FLAD1* expression with optimal cutoffs defined by the surv_cutpoint function. **f** Tumor *FLAD1* expression in patients with partial response or progressive disease to immunotherapy (Fudan Cohort, $n = 17$). **g** Proportions of *FLAD1*$^+$ tumor cells in patients with partial response or stable disease (Immunotherapy Cohort, $n = 8$). **h** Subcutaneous tumors were established in C57BL/6 mice with Hepa1-6 cells (Ctrl or sh*Flad1*, $n = 5$ per group). Tumor volumes were measured at the indicated timepoints. Tumors were photographed and weighed at day 21. **i**, **j** Orthotopic tumors were established in C57BL/6 mice with Hepa1-6 cells (Ctrl or sh*Flad1*, $n = 6$ per group). Livers were photographed and weighed at day 21 (**i**). Bioluminescence imaging was used to visualize tumors at days 14 and 21 (**j**). **k** Subcutaneous tumors in *Rag1*$^{-/-}$ mice with Hepa1-6 cells (Ctrl or sh*Flad1*, $n = 6$ per group). Tumor volumes were measured at the indicated timepoints. Tumors were photographed and weighed at day 21. **l**, **m** Orthotopic tumors in *Rag1*$^{-/-}$ mice with Hepa1-6 cells (Ctrl or sh*Flad1*, $n = 5$ per group). Livers were photographed and weighed at day 21 (**l**). Bioluminescence imaging was used to visualize tumors at days 14 and 21 (**m**). Data are presented as mean ± SD (**f**–**h**, **i**, **k**, **l**) or median with interquartile ranges (**d**). *P*-values were calculated using two-way ANOVA with Tukey's test (**h**, **k**), unpaired two-sided Student's *t* test (**f**, **k**, **l**), two-sided Wilcoxon signed-rank test (**d**), two-sided Wilcoxon rank-sum test (**g**–**i**), and log-rank test (**e**). Source data are provided as a Source Data file.

C06, C05, C03, C02, C01) exhibited significant features of T cell exhaustion (Fig. 3g), indicating a majority of intratumoral CD8$^+$ T cells are in an exhausted state, consistent with human HCC observations[19]. scDist analysis revealed pronounced perturbations in most subsets of CD8$^+$ T cells following FADS knockdown (Fig. 3h). We next evaluated CD8$^+$ T cell function using gene signatures for interferon (IFN), dysfunction, and proliferation (see Supplementary Data. 3). Nearly all CD8$^+$ T cell subsets in FADS-knockdown tumors exhibited improved cytotoxicity, reduced exhaustion, and enhanced proliferation compared to those in control tumors (Supplementary Fig. 10a). Collectively, FADS knockdown led to more cytotoxic and proliferative CD8$^+$ T cells with decreased dysfunction (Fig. 3i). Enrichment analysis of CD8$^+$ T cells demonstrated upregulation of ligand-receptor signaling, T cell activation, chemokine, cytokine, and intracellular signal transduction (Fig. 3j and Supplementary Fig. 10b, c).

In summary, FADS exerts profound influences on both tumor cells and CD8$^+$ T cells within the TME, and loss of FADS reshapes the immunosuppressive TME.

FADS knockdown increases CD8$^+$ T cell infiltration

To investigate how tumor cell FADS influenced CD8$^+$ T cells, we noted that "chemokine signaling pathway" was significantly enriched in both tumor cells and CD8$^+$ T cells according to our scRNA-seq analysis (Fig. 3e, j). To further validate, we performed bulk RNA-seq on FADS-knockdown and control Hep3B cells. Gene set enrichment analysis (GSEA) confirmed that the "chemokine receptors bind chemokines" pathway was significantly upregulated in FADS-knockdown cells (Fig. 4a), suggesting that FADS may regulate CD8$^+$ T cell recruitment through chemokine signaling.

We then examined the TCGA-LIHC and OPE000321 datasets, and found that higher *FLAD1* expression was correlated with a reduced CD8T gene signature (defined in Supplementary Data. 3) in both cohorts (Fig. 4b). Consistently, tissue microarray analysis revealed that tumors with higher FADS expression had fewer intratumoral CD8$^+$ T cells (Fig. 4c, d). Supporting these results, both subcutaneous and orthotopic mouse models showed significantly increased infiltration of CD8$^+$ T cells in FADS-knockdown tumors compared to controls (Fig. 4e). In addition, flow cytometry analysis showed that CD8$^+$ T cells from Fads-knockdown tumors had higher IFNγ (cytotoxicity marker) and lower PD-1 (exhaustion marker) expression compared to control tumors (Fig. 4f and Supplementary Fig. 11), consistent with the scRNA-seq data. Taken together, these findings indicate that FADS inhibits the recruitment of CD8$^+$ T cells in HCC.

FADS inactivates tumor-intrinsic cGAS-STING pathway to impede CD8$^+$ T cells recruitment

To understand how FADS disrupted chemokine signaling and impaired CD8$^+$ T cell recruitment, we investigated the underlying molecular mechanisms. Bulk RNA-seq analysis revealed upregulated pathways of "DNA double-strand break response" and "DNA damage checkpoint" in FADS-knockdown Hep3B cells (Fig. 4g). Previous studies have shown that DNA damage in cancer cells can activate the cGAS-STING pathway, leading to the production of type I IFNs and chemokines, thereby enhancing CD8$^+$ T cell recruitment and tumor elimination (Fig. 4h)[20–22]. However, the cGAS-STING pathway are frequently inactivated in tumors, as it is a strategy employed by cancer cells to evade immune surveillance and promote tumor progression. Reactive oxygen species (ROS) are a major source of DNA damage[23]. Given the key role of VB2 metabolism in maintaining antioxidant defenses[24], we speculated that loss of FADS could upregulate ROS levels. Supporting this, elevated ROS was observed in FADS-knockdown Hep3B cells (Fig. 4i). We therefore proposed that FADS might reduce ROS-induced DNA damage, thereby suppressing cGAS-STING activation and downstream chemokines. Our scRNA-seq data supported the hypothesis, demonstrating significant upregulation of "response to IFN-β," "response to type I IFN," and "chemotaxis" pathways in CD8$^+$ T cells following FADS knockdown (Supplementary Fig. 10c).

To validate the mechanism, we assessed DNA damage using γH2AX staining, which was markedly elevated in FADS-knockdown Hep3B cells (Fig. 4j). Cytosolic double-stranded DNA (dsDNA), necessary for cGAS-STING activation, was more evident in FADS-knockdown cells compared to control cells (Fig. 4k). Western blot analysis showed that FADS knockdown led to increased phosphorylation of TBK1 (Ser172) and IRF3 (Ser396) (Fig. 4l), indicating activation of the cGAS-STING pathway. In addition, FADS knockdown significantly upregulated the expression of downstream IFN-stimulated genes (*ISG15*, *IFIT1*, *IFNB1*) and chemokine genes (*CCL5*, *CXCL9*, *CXCL10*) (Fig. 4m), corroborating the enhanced chemokine signaling. Rescue experiments further showed that treatment with FAD or the STING inhibitor H-151 reversed the upregulated gene expression caused by FADS knockdown (Fig. 4m), confirming that FADS negatively regulates the cGAS-STING pathway.

In summary, FADS alleviates ROS-induced DNA damage, thereby suppressing cGAS-STING activation and downstream chemokine signaling, ultimately reducing CD8$^+$ T cell infiltration and antitumor immunity in HCC.

FADS knockdown triggers ferroptosis in HCC cells

Loss of FADS inhibited HCC cell growth, with the underlying mechanism requiring further investigation. Our scRNA-seq analysis revealed that enrichment of cell death-related and metabolic pathways in FADS-knockdown tumor cells (Fig. 3e). Notably, pronounced cell death was observed in FADS-knockdown HCC cells, with cell membrane rupture (Fig. 5a). To further dissect metabolic changes, we conducted untargeted metabolomics on FADS-knockdown Hep3B cells. Differentially expressed metabolites are listed in Supplementary Data. 4. Consistent with its enzymatic role, FADS knockdown resulted in increased VB2 levels, decreased FAD levels, and no significant

https://doi.org/10.1038/s41467-025-64572-y

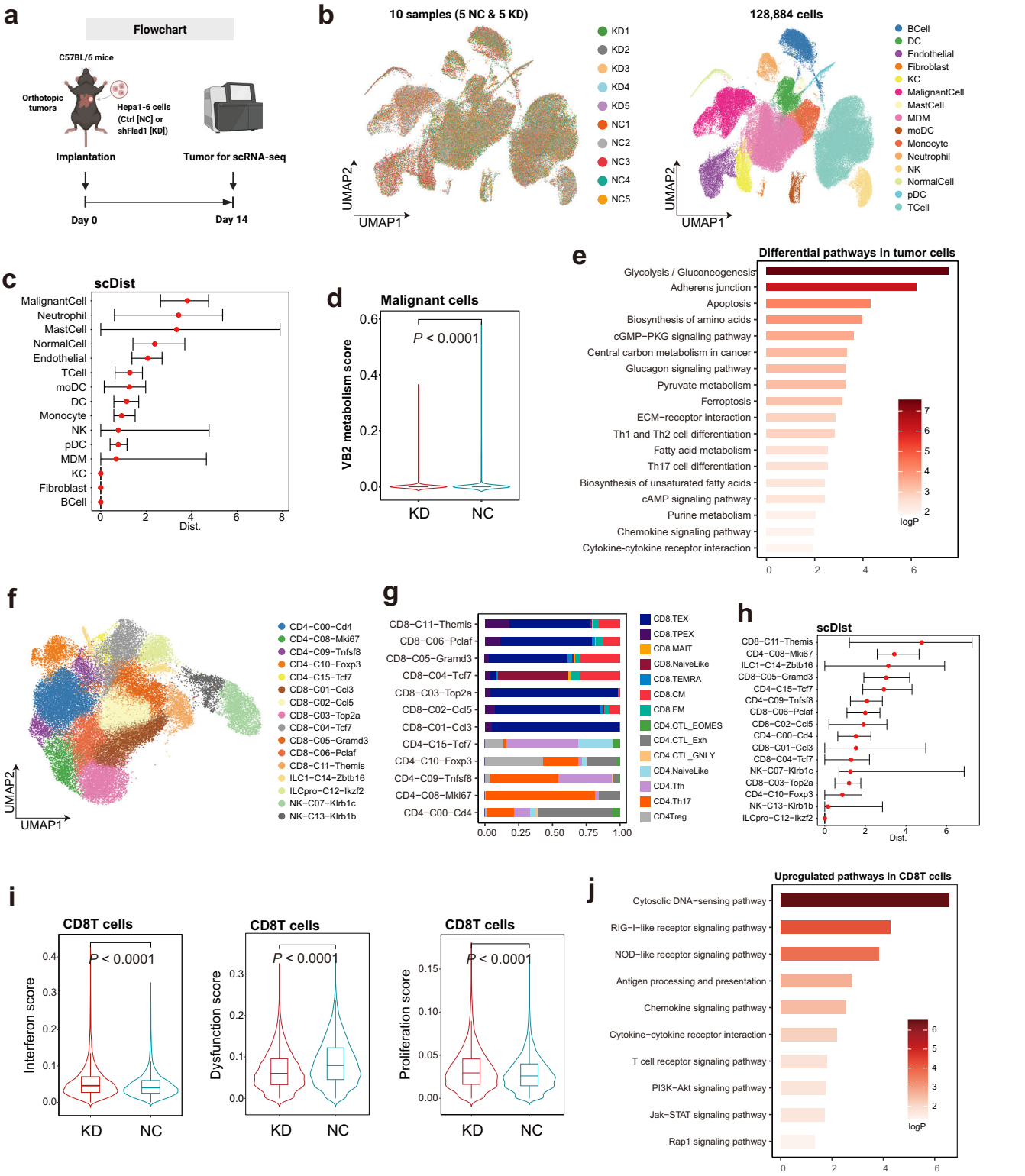

Fig. 3 | Single-cell RNA-seq analysis reveals the impact of FADS on tumor microenvironment. a Workflow of single-cell RNA-seq analysis for mouse tumors (created in BioRender. Chao, J. (2025) https://BioRender.com/bpec5ea). Orthotopic tumors were established in C57BL/6 mice with Hepa1-6 cells (Ctrl or sh*Flad1*, $n = 5$ per group). Tumors were harvested at day 14 for single-cell RNA-seq. **b** UMAP plots showing the distribution of 10 tumor samples (5 NC [control] vs. 5 KD [Fads knockdown]) and 15 major cell types. **c** scDist analysis ranking perturbation levels in major cell types between NC and KD groups, displayed as effect values (red dot) with 95% confidence intervals. **d** Violin plot showing VB2 metabolism scores in malignant cells between NC and KD groups. **e** KEGG pathway enrichment analysis of differentially expressed genes in tumor cells (KD vs. NC). **f** UMAP plot showing the distribution of 16 T & NK lymphocytes subsets. **g** Annotation of T cell subsets based on canonical T cell gene signatures. Bars illustrate the composition of various T cell subsets. **h** scDist analysis ranking perturbation levels across T & NK lymphocytes subsets between NC and KD groups, with effect values (red dot) and 95% confidence intervals. **i** Interferon, dysfunction, and proliferation scores (AUCell algorithm) in $CD8^+$ T cells from NC and KD groups. The box shows the median with interquartile ranges (IQR), whiskers extend to 1.5 × IQR, and no outliers were plotted. **j** KEGG pathway enrichment analysis of upregulated genes in $CD8^+$ T cells (KD vs. NC). *P*-values were calculated using a two-sided Wilcoxon rank-sum test (**d**, **i**).

https://doi.org/10.1038/s41467-025-64572-y

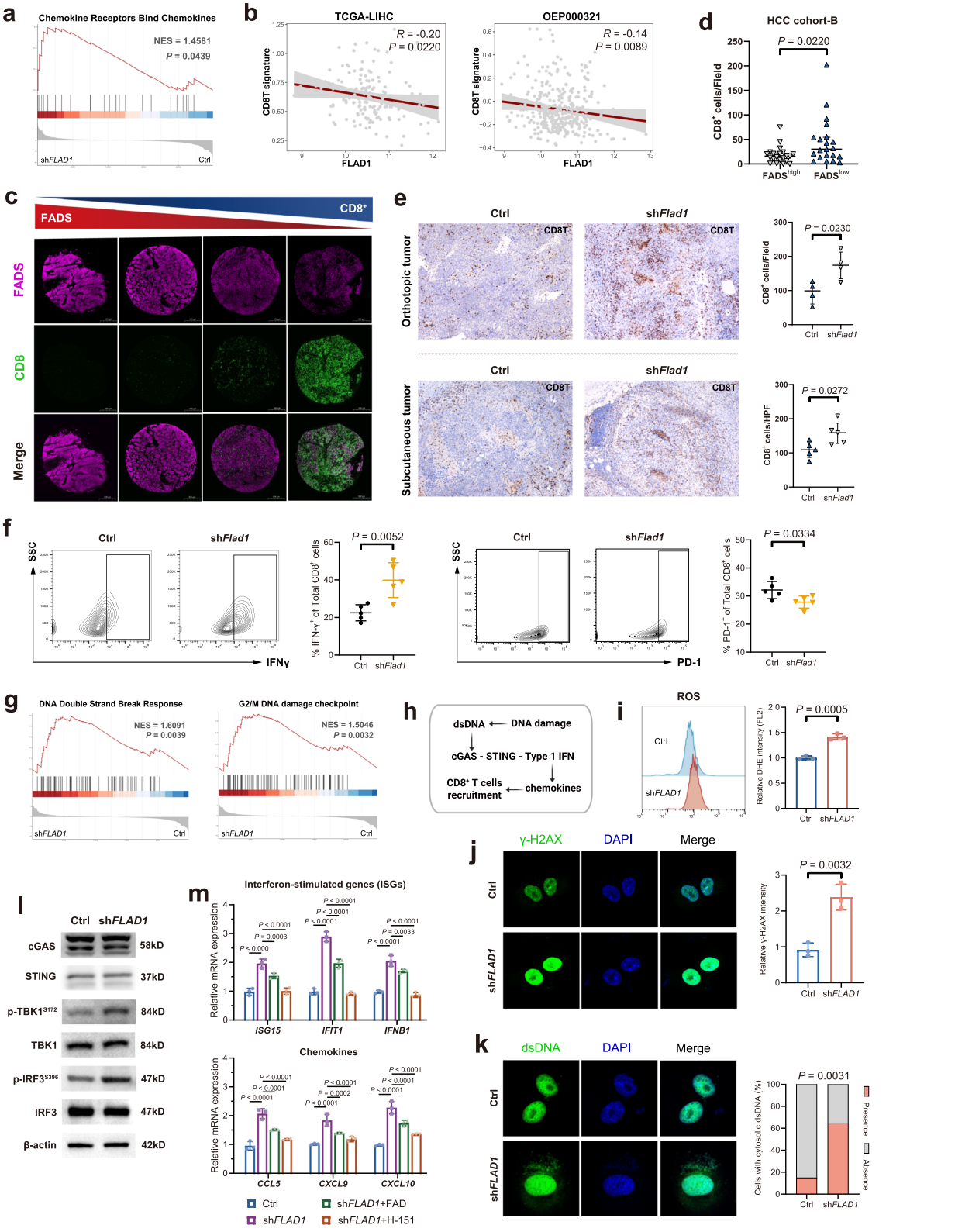

change in FMN levels (Fig. 5b). KEGG enrichment analysis identified "biosynthesis of unsaturated fatty acids" pathway as the most significantly affected pathway (Fig. 5c), which was also highlighted in the scRNA-seq results (Fig. 3e). Specifically, all differentially expressed metabolites within this pathway were polyunsaturated fatty acids (PUFAs), and their levels were elevated after FADS knockdown (Fig. 5d). Moreover, reduced glutathione (GSH) levels were significantly decreased (Fig. 5e). Given that cell death with membrane rupture, increased PUFAs, decreased GSH and elevated ROS are hallmarks of ferroptosis[25], these findings pointed that FADS knockdown may trigger ferroptosis. Supporting this, lipid peroxidation, a key marker of ferroptosis, was significantly increased following FADS knockdown (Fig. 5f). Moreover, treatment with Ferrostatin-1 (ferroptosis inhibitor) restored the decreased cell viability caused by FADS knockdown, whereas FADS overexpression reduced the loss of cell viability caused by Erastin (ferroptosis inducer) (Fig. 5g). Together,

Fig. 4 | FADS inactivates the cGAS-STING pathway to impede CD8⁺ T cell recruitment. a Gene set enrichment analysis showing upregulation of the "Chemokine receptors bind chemokines" pathway in Hep3B cells following FADS knockdown. **b** Correlation analyses between *FLAD1* expression and CD8⁺ T cell signature scores in TCGA-LIHC and OEP000321 datasets. **c**, **d** Representative images of FADS and CD8 staining in tumors from Cohort-B (**c**), and quantification of CD8⁺ T cell density ($n = 42$ patients) (**d**). FADS expression level was stratified by median H-score (high vs. low). **e** Representative images of CD8 staining in orthotopic and subcutaneous Hepa1-6 tumors, and quantification of CD8⁺ T cell density in orthotopic tumors ($n = 4$ per group) and subcutaneous tumors ($n = 5$ per group). **f** Percentages of IFN-γ⁺ and PD-1⁺ cells among CD8⁺ T cells in subcutaneous Hepa1-6 tumors ($n = 5$ per group), as determined by flow cytometry. **g** Upregulation of "DNA double-strand break response" and "DNA damage checkpoint" pathways in Hep3B cells following FADS knockdown. **h** Schematic illustration of DNA damage-induced cGAS-STING pathway activation. **i** Reactive oxygen species (ROS) levels in Hep3B cells ($n = 3$ biological replicates). **j** Representative immunofluorescence (IF) images and quantitative analysis of γH2AX staining in Hep3B cells ($n = 3$ biological replicates). **k** Representative IF images and qualitative analysis of double-stranded DNA (dsDNA) staining in Hep3B cells ($n = 20$ biological replicates). **l** Western blots showing the expression of key proteins in the cGAS-STING pathway in Hep3B cells ($n = 3$ independent experiments). **m** Relative mRNA levels of interferon-stimulated genes (*ISG15*, *IFIT1*, *IFNB1*) and chemokines (*CCL5*, *CXCL9*, *CXCL10*) in Hep3B cells ($n = 3$ biological replicates). FAD, 20 μM for 48 h; H-151 (STING inhibitor), 1 μM for 12 h. Data are presented as mean ± SD (**e**, **f**, **i**, **j**, **m**) or median with interquartile ranges (**d**). *P*-values were calculated using unpaired two-sided Student's *t* test (**e**, **f**, **i**, **j**, **m**), two-sided Wilcoxon rank-sum test (**d**), Fisher's exact test (**k**), and Spearman's rank correlation (**b**). Source data are provided as a Source Data file.

these results demonstrate that FADS promotes resistance against ferroptosis, and its loss induces ferroptosis.

To determine if these findings extend beyond HCC, we performed additional experiments in the breast cancer cell line MDA-MB-468 and the lung cancer cell line A549. In both lines, FADS knockdown inhibited colony formation, increased cell death, and elevated ROS and lipid peroxidation levels (Supplementary Fig. 12), consistent with the findings in HCC cells. These results underscore the broader significance of FADS in cancer biology.

FADS confers ferroptosis resistance via enzymatic activity-dependent FAD production

GSH plays a pivotal role in ferroptosis resistance by detoxifying peroxides[25]. Glutathione reductase (GR) is a flavoprotein enzyme that requires FAD as a coenzyme to regenerate GSH from oxidized glutathione (GSSG) (Fig. 5h)[24]. Since FADS knockdown reduced both FAD and GSH levels, we speculated that GR activity might be impaired. Indeed, GR activity was significantly decreased reduced in FADS-knockdown cells, and supplement with FAD could restore its activity (Fig. 5i). Correspondingly, supplement with FAD also rescued GSH levels and GSH/GSSG ratio, as well as suppressed the elevated ROS and lipid peroxidation observed after FADS knockdown (Fig. 5j). Importantly, supplement with FAD prevented cell death caused by FADS knockdown (Fig. 5k). Notably, only FAD, but not VB2 or FMN, was able to restore the decreased cell viability caused by FADS knockdown (Fig. 5l).

These findings demonstrate that FADS confers ferroptosis resistance in HCC cells via its enzymatic role in FAD production. FAD is essential for maintaining GR activity and GSH levels, thereby inhibiting lipid peroxidation and protecting cells from ferroptosis.

FADS inhibits ferroptosis by interacting with PCBP2

During ferroptosis, the lipid peroxidation is also driven by the labile iron pool, namely intracellular Fe^{2+} levels[25]. Intriguing, Fe^{2+} levels was increased following FADS knockdown (Fig. 6a), despite FADS not being directly involved in iron metabolism. We hypothesized FADS might interact with an iron-regulatory protein to modulate the process. To identify the iron-regulatory protein that interacts with FADS, we performed immunoprecipitation (IP) of FADS-binding proteins followed by mass spectrometry (MS), which identified 387 candidates (Supplementary Data. 5). We focused on iron-regulatory proteins and found that Poly(rC)-binding protein 2 (PCBP2) was the top-ranked candidate (Fig. 6b). PCBP2 functions as an Fe^{2+} chaperone, and its loss increases labile iron pool and triggers ferroptosis[26–28]. We thus hypothesized that FADS may regulate ferroptosis by interacting with PCBP2.

Co-IP confirmed the interaction between FADS and PCBP2 (Fig. 6c), and immunofluorescence analysis demonstrated their colocalization in the cytoplasm (Fig. 6d). Notably, FADS knockdown did not affect PCBP2 mRNA levels but significantly reduced its protein expression (Fig. 6e and Supplementary Fig. 13a). Moreover, IHC analysis in tumors revealed a strong positive correlation between FADS and PCBP2 expression ($R = 0.598$, $P < 0.001$; Fig. 6f). In rescue experiments, PCBP2 overexpression in FADS-knockdown HCC cells reduced the Fe^{2+} levels and prevented tumor cell death (Fig. 6g). In mouse models, Pcbp2 overexpression also significantly reversed the tumor regression observed in Fads-knockdown tumors (Fig. 6h).

In summary, FADS interacts with PCBP2 and is required to maintain PCBP2 protein stability, thereby conferring ferroptosis resistance in HCC cells.

FADS reduces PCBP2 ubiquitination and degradation via non-enzymatic function

To delineate the interaction domains of FADS and PCBP2, we constructed truncated FADS and PCBP2 plasmids and transfected them into 293T cells (Fig. 6i). Co-IP demonstrated that FADS C-terminus bound to PCBP2 (Fig. 6j), and PCBP2 KH1 domain bound to FADS (Fig. 6k). Protein docking simulations suggested that Thr389, Gln393, and Cys499 in FADS C-terminus interacted with Val12, Thr15, and Thr65 in PCBP2 KH1 domain (Fig. 6l). To validate these predicted interactions, we generated FADS and PCBP2 mutation plasmids using site-directed mutagenesis, in which the three target amino acids were simultaneously substituted with alanine (Supplementary Fig. 13b). Co-IP revealed that mutation of Val12, Thr15, and Thr65 in PCBP2 abolished its interaction with FADS, and mutation of Thr389, Gln393, and Cys499 in FADS abrogated its binding to PCBP2 (Fig. 6m), confirming the specific interaction sites between FADS and PCBP2.

We next investigated how FADS regulates PCBP2 expression. In the presence of cycloheximide (CHX), PCBP2 degradation was accelerated in FADS-knockdown Hep3B cells and delayed in FADS-overexpressing cells (Fig. 6n), indicating that FADS promotes PCBP2 protein stability. Treatment with MG132 (protease inhibitor) reversed the downregulation of PCBP2 induced by FADS knockdown (Fig. 6o), suggesting that FADS prevents PCBP2 degradation via the proteasome pathway. Moreover, FADS knockdown enhanced PCBP2 ubiquitination, whereas FADS overexpression reduced it (Fig. 6p), implicating FADS negatively regulates PCBP2 ubiquitination. Since FADS cannot remove ubiquitin, we hypothesized that it recruits a deubiquitinase to mediate the process. Among the IP-MS results (Supplementary Data. 5), ubiquitin-specific peptidase 10 (USP10) was the only deubiquitinase. Co-IP confirmed USP10 interacted with both FADS and PCBP2 (Fig. 6q). In the complex, FADS acts as an adapter to facilitate the interaction between PCBP2 and USP10 (Fig. 6r).

Collectively, we uncover another mechanism by which FADS regulates ferroptosis independent of its enzymatic activity. FADS recruits USP10 to deubiquitinate and stabilize PCBP2, thereby maintaining intracellular Fe^{2+} homeostasis and impeding ferroptosis.

Hesperidin is identified as a potential FADS inhibitor

Currently, there are no available FADS inhibitors. To address this gap, we conducted structure-based high-throughput virtual

https://doi.org/10.1038/s41467-025-64572-y

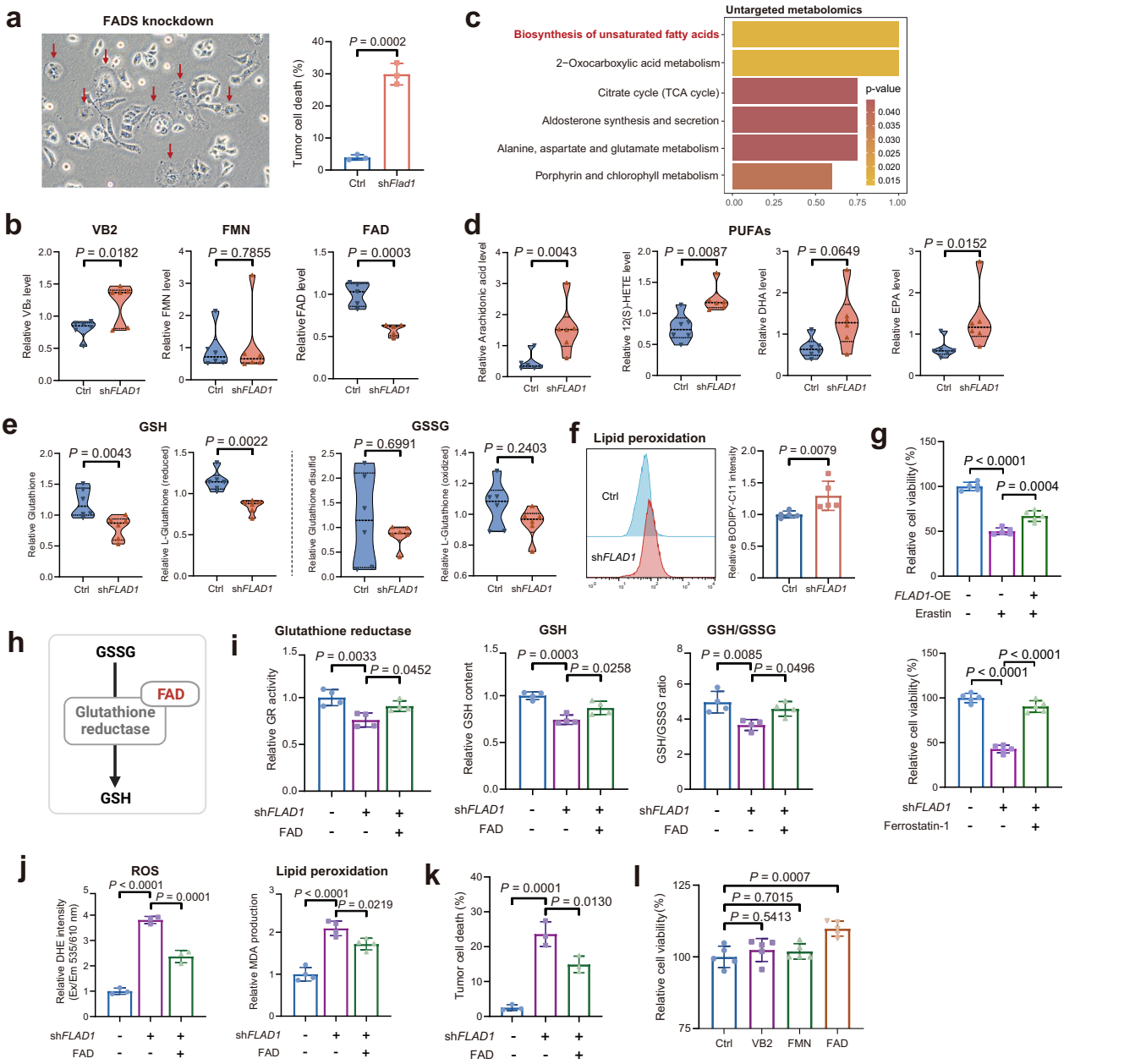

Fig. 5 | FADS produce FAD to inhibit ferroptosis. a Representative image of cell death in Hepa1-6 cells following Fads knockdown ($n = 3$ biological replicates). The percentage of dead cells (7-AAD$^+$) were analyzed via flow cytometry. **b** Relative intracellular levels of VB2, FMN, and FAD in Hep3B cells. VB2 and FMN detected by untargeted metabolomics ($n = 6$ biological replicates); FAD measured by a fluorescence probe ($n = 5$ biological replicates). **c** KEGG enrichment analysis of differentially expressed metabolites in Hep3B cells (Ctrl vs. sh*FLAD1*). **d** Relative intracellular levels of arachidonic acid, 12(S)-HETE, docosahexaenoic acid (DHA), and eicosapentaenoic acid (EPA) in Hep3B cells detected in untargeted metabolomics ($n = 6$ biological replicates). **e** Relative intracellular levels of glutathione (GSH) and oxidized glutathione (GSSG) in Hep3B cells, assessed by untargeted metabolomics ($n = 6$ biological replicates). **f** Lipid peroxidation in Hep3B cells, detected using BODIPY 581/591 C11 via flow cytometry ($n = 5$ biological replicates). **g** Cell viability of Hep3B cells with FADS overexpression treated with Erastin (20 μM), or with FADS knockdown treated with Ferrostatin-1 (10 μM), as determined by CCK-8 assay ($n = 5$ biological replicates). **h** Schematic illustration of FAD serving as a coenzyme to assist glutathione reductase (GR) in converting GSSG to GSH. **i** GR activity, GSH levels, and GSH/GSSG ratio in Hep3B cells ($n = 4$ biological replicates). FAD, 20 μM for 48 h. **j** Levels of ROS and lipid peroxidation in Hep3B cells ($n = 3$ biological replicates). FAD, 20 μM for 48 h. **k** Percentage of dead cells (7-AAD$^+$) in Hep3B cells following indicated treatments ($n = 3$ biological replicates). FAD, 20 μM for 48 h. **l** Hep3B cells with FADS-knockdown treated with VB2 (10 μM), FMN (10 μM), FAD (10 μM), or PBS (Ctrl) for 48 h, followed by CCK-8 assay ($n = 5$ biological replicates). Data are presented as mean ± SD (**a**, **f**, **g**, **i**, **j**, **k**, **l**) or median with interquartile ranges (**b**, **d**, **e**). *P*-values were calculated using unpaired two-sided Student's *t* test (**a**, **b**, **f**, **g**, **i**, **j**, **k**, **l**), and two-sided Wilcoxon rank-sum test (**d**, **e**, **f**). Source data are provided as a Source Data file.

screening using the ChemDiv database (1,583,358 compounds) to search potential FADS inhibitors (Fig. 7a). The binding pocket was set at the FADS C-terminus, containing the enzymatic catalytic center. After three screening rounds and applying a threshold of docking scores greater than 10, we narrowed the selection to 26 top-ranked compounds. Among these, five compounds were commercially available and mass-produced, which were chosen for experimental validation (Fig. 7b). Hesperidin demonstrated the most efficient effect on inhibiting cell proliferation among the five selected compounds (Fig. 7c, d). Hesperidin, a flavonoid

https://doi.org/10.1038/s41467-025-64572-y

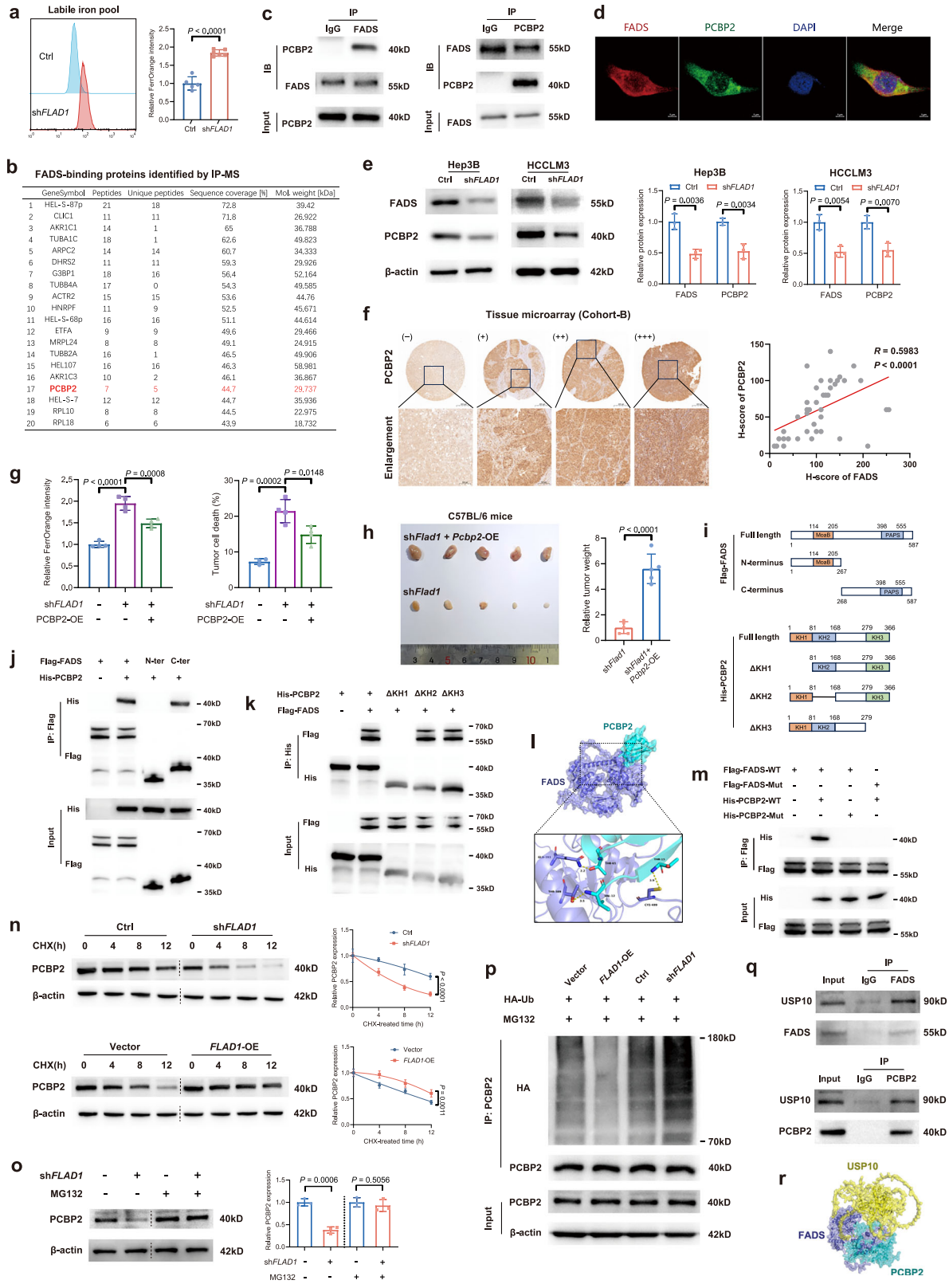

abundant in citrus fruits, has demonstrated efficacy in multiple preclinical models of tumors, inflammation, and cardiovascular diseases[29,30]. Clinically, Hesperidin is an active ingredient in approved pharmaceutical products. For example, micronized purified flavonoid fractions (MPFF) containing Hesperidin and Diosmin have been recommended for venous insufficiency and hemorrhoidal disease[31,32].

The inhibitory effect of Hesperidin on HCC cell proliferation was confirmed by colony formation assays (Fig. 7e). In subcutaneous models, Hesperidin treatment significantly suppressed tumor growth and reduced tumor weight compared to the control group in *Rag1*$^{-/-}$ mice (Fig. 7f), with an even stronger effect observed in C57BL/6 mice (Fig. 7g). In addition, Hesperidin treatment also led to increased infiltration of intratumoral CD8^{+} T cells in C57BL/6 mice (Fig. 7m).

Fig. 6 | FADS stabilize PCBP2 to inhibit ferroptosis. a Intracellular Fe^{2+} levels in Hep3B cells ($n = 5$ biological replicates). **b** Identification of FADS-binding proteins in Hep3B cells using immunoprecipitation (IP) and mass spectrometry. The top 20 candidates are ranked by sequence coverage. **c** Co-IP assay showing the interaction between FADS and PCBP2 in Hep3B cells ($n = 3$ independent experiments). **d** IF staining showing co-localization of FADS and PCBP2 in Hep3B cells. **e** Protein levels and quantification of FADS and PCBP2 in Hep3B and HCCLM3 cells ($n = 3$ biological replicates). **f** Representative images of PCBP2 staining in tumor samples from Cohort-B, and correlation analysis of FADS and PCBP2 protein levels. **g** Intracellular Fe^{2+} levels and percentages of dead cells (7-AAD$^+$) in Hep3B cells following FADS knockdown with or without PCBP2 overexpression (OE) ($n = 3$ biological replicates). **h** Subcutaneous tumors in C57BL/6 mice ($n = 5$ per group) with Hepa1-6 cells (sh*Flad1* vs. sh*Flad1* + *Pcbp2*-OE). Tumors were photographed and weighed at day 21. **i** Diagram of truncated plasmids encoding FLAG-tagged FADS and His-tagged PCBP2. **j**, **k** 293T cells were transfected with truncated plasmids of FADS and PCBP2. Co-IP assays indicated that the FADS C-terminus binds to PCBP2 (**j**), and the PCBP2 KH1 domain binds to FADS (**k**) ($n = 3$ independent experiments). **l** Docking analysis revealing specific binding sites between FADS and PCBP2. **m** Mutation of the binding interface between FADS and PCBP2 by replacing target amino acids with alanine disrupts their interaction, as shown by Co-IP assay ($n = 3$ independent experiments). WT, wide-type; Mut, mutation. **n** Protein levels and quantification of PCBP2 in Hep3B cells with FADS knockdown or overexpression ($n = 3$ biological replicates). Cells were treated with cycloheximide (CHX, 50 μg/mL) for the indicated times. **o** Protein levels and quantification of PCBP2 in Hep3B cells treated with or without MG132 (20 μM, 12 h) ($n = 3$ biological replicates). **p** PCBP2 ubiquitination (Ub) levels in Hep3B cells with FADS knockdown or overexpression ($n = 3$ independent experiments). **q** Co-IP assay showing interactions between USP10 and FADS, and USP10 and PCBP2 ($n = 3$ independent experiments). **r** Docking model of FADS, PCBP2, and USP10. Data are presented as mean ± SD (**a**, **e**, **g**, **h**, **n**, **o**). *P*-values were calculated using unpaired two-sided Student's *t* test (**a**, **e**, **g**, **h**, **o**), two-way ANOVA with Tukey's test (**n**), and Spearman's rank correlation (**f**). Source data are provided as a Source Data file.

Moreover, Hesperidin treatment showed no evidence of organ toxicity, as confirmed by histopathology and serum biochemical analyses (Supplementary Fig.14).

Molecular docking analysis revealed that Hesperidin binds to FADS C-terminus at Tyr354, Tyr536, and Ile538 (Fig. 7h), with a binding energy of − 9.4 kcal/mol, indicating a strong interaction. Functionally, Hesperidin treatment significantly reduced intracellular FAD levels, confirming its inhibition of FADS enzymatic activity (Fig. 7i). In addition, Hesperidin increased ROS levels, promoted lipid peroxidation, and induced tumor cell death (Fig. 7j–l). Supplementation with FAD reversed these effects, demonstrating that Hesperidin-induced ferroptosis is mediated through FADS inhibition.

In summary, we identified FADS as a target of Hesperidin. Hesperidin inhibits FADS enzymatic activity, triggers ferroptosis, and demonstrates potent antitumor effects, highlighting its potential as a therapeutic candidate for HCC.

Discussion

Several epidemiological studies have explored the relationship between VB2 and cancer. A prospective cohort study involving 120,852 participants demonstrated an inverse correlation between dietary VB2 intake and the risk of proximal colon cancer[33]. Another study involving 63,257 participants revealed a dose-dependent association between increased serum VB2 levels and pancreatic cancer risk[34]. These results suggest that VB2 metabolism has a complex, context-dependent role in different cancers. In this study, we demonstrated that VB2 metabolism promoted HCC progression.

RFK and FADS are key enzymes in VB2 metabolism, with RFK being considered the rate-limiting enzyme in normal tissues[6]. Several studies explored the role of VB2 metabolism in macrophages and highlighted the role of RFK in regulating polarization and phagocytosis of macrophages[35,36]. However, our data showed that FADS, rather than RFK, was widely overexpressed in HCC, positioning FADS as the governor of VB2 metabolism in HCC. Mechanistically, FADS conferred ferroptosis resistance in HCC cells through enzymatic activity-dependent and -independent manners. First, its enzymatic activity facilitated FAD production, which maintained GR activity and GSH levels. Second, FADS stabilized PCBP2 via its non-enzymatic function to reduce Fe^{2+} levels and the labile iron pool. Beyond its effects on tumor cell itself, FADS also impacts $CD8^+$ T cells, ultimately suppressing T cell-mediated antitumor immunity.

PCBP2 is frequently overexpressed in various cancers and contributes to tumor development and progression[37]. PCBP2 could act as an iron chaperone, both as a receiver from the iron importer DMT1 and as a donor to the iron exporter FPN1s[26,27]. In cancer cells, PCBP2 has been reported to regulate ferroptosis by directly affecting Fe^{2+} levels[28]. Alternatively, PCBP2 also acts as an RNA-binding protein that regulates ferroptosis. Shen et al. reported that PCBP2 binds to *SLC7A11* mRNA, delaying its degradation, and PCBP2 knockdown leads to decreased SLC7A11 expression[38]. As SLC7A11 is a key inhibitor of ferroptosis that promotes cystine uptake, essential for glutathione synthesis and cellular antioxidant defense[25], PCBP2 knockdown ultimately increases cellular susceptibility to ferroptosis[38].

To enhance therapeutic potential, we identified Hesperidin as a potential FADS inhibitor. Hesperidin is a natural flavonoid with demonstrated antitumor properties in various cancers[29,39]. Hesperidin has been reported to inhibit hepatocarcinogenesis in rat models and induce cell cycle arrest and apoptosis in HCC cells[29,39]. In this work, Hesperidin induced ferroptosis in HCC cells by targeting FADS. Although preclinical and some clinical studies have established the efficacy and safety of Hesperidin under various conditions, there is a lack of clinical data on cancer patients, and further rigorous studies are required.

In conclusion, FADS facilitates HCC progression through two major mechanisms (Fig. 8): (i) promoting ferroptosis resistance in tumor cells to support tumor growth; and (ii) inhibiting $CD8^+$ T cell recruitment, thereby dampening antitumor immunity. Our study highlights FADS as a promising therapeutic target in HCC.

Methods

Human specimens

Three HCC cohorts were included in this study, with patient characteristics detailed in Supplementary Data. 1. The immunotherapy Cohort included 8 HCC patients receiving anti-PD-1 therapy. Baseline tumor biopsy samples were collected prior to treatment and subjected to single-cell RNA sequencing (scRNA-seq). Inclusion criteria: (i) unresectable advanced HCC, (ii) treatment with PD-1 inhibitors for at least two cycles, and (iii) ECOG-PS of 0–2. Treatment responses were evaluated using the modified Response Evaluation Criteria in Solid Tumors (mRECIST) criteria, and were classified as complete response, partial response, stable disease, and progressive disease. Cohort-A ($n = 30$) and Cohort-B ($n = 42$) comprised 72 HCC patients who underwent liver resection. Patients with prior antitumor therapy, recurrent HCC, or ruptured tumors were excluded. Tumor and adjacent liver tissues from Cohort-A were used for RNA and protein extraction, while samples from Cohort-B were used for tissue microarray construction. Specimens were collected at Peking Union Medical College Hospital (PUMCH), Beijing, China, under ethical approval from the PUMCH Ethics Committee (No. JS-2296). Written informed consent was obtained from all participants, and the study adhered to the 1975 Declaration of Helsinki guidelines.

Mice

Wild-type C57BL/6 mice (C57BL/6JGpt, male, 5–6 weeks old, #N000013) and *Rag1*$^{-/-}$ C57BL/6 mice (C57BL/6JGpt-*Rag1*^{em1Cd3259}/Gpt, male, 5–6 weeks old, #T004753) were purchased from

https://doi.org/10.1038/s41467-025-64572-y

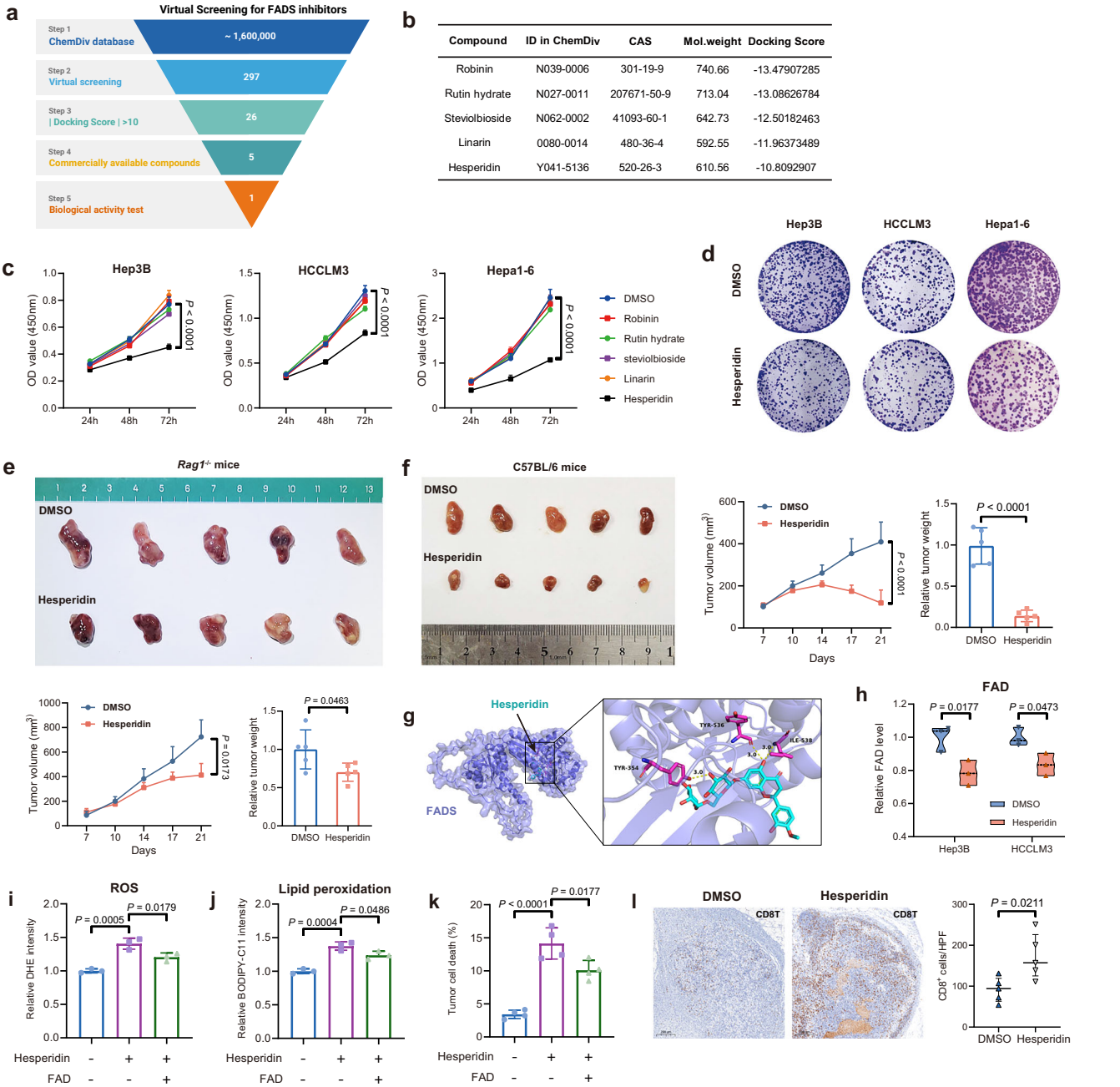

Fig. 7 | Hesperidin is identified as a FADS inhibitor. a Workflow for high-throughput virtual screening of FADS-targeting compounds. **b** Five compounds selected for experimental validation. **c** Proliferation of Hep3B, HCCLM3 and Hepa1-6 cells treated with the five compounds (100 μM) respectively, as determined by CCK-8 assay ($n = 5$ biological replicates). **d** Colony formation of Hep3B, HCCLM3 and Hepa1-6 cells following Hesperidin (100 μM) treatment. **e**, **f** Subcutaneous tumors generated by Hepa1-6 cells in *Rag1*$^{-/-}$ mice (**e**) and C57BL/6 mice (**f**) ($n = 5$ per group). Hesperidin (100 mg/kg) or DMSO control was administered daily by intraperitoneal injection. Tumor volumes were measured at the indicated time-points. Tumors were photographed and weighed at day 21. **g** Docking analysis showing the interaction between Hesperidin and FADS. **h** FAD levels in Hep3B and HCCLM3 cells treated with or without Hesperidin (100 μM, 48 h) ($n = 3$ biological replicates). **i**, **j** ROS and lipid peroxidation in Hep3B cells treated as indicated ($n = 3$ biological replicates). Hesperidin, 100 μM for 48 h; FAD, 20 μM for 48 h. **k** Percentage of dead cells (7-AAD$^+$) in Hep3B cells ($n = 4$ biological replicates). Hesperidin, 100 μM for 48 h; FAD 20 μM for 48 h. **l** Representative images and quantification of CD8$^+$ T cell density in subcutaneous Hepa1-6 tumors treated with or without Hesperidin ($n = 5$ per group). Data are presented as mean ± SD (**c**, **e**, **f**, **i**, **j**, **k**, **l**) or median with interquartile ranges (**h**). *P*-values were calculated using unpaired two-sided Student's *t* test (**e**, **f**, **h**, **i**, **j**, **k**, **l**), and two-way ANOVA with Tukey's test (**c**, **e**, **f**). Source data are provided as a Source Data file.

GemPharmatech Co., Ltd. (Jiangsu, China). Mice were housed under specific pathogen-free conditions with a standard chow diet, and were maintained at a room temperature of 20–26 °C on a 12 h light/12 h dark cycle. All experimental protocols were approved by the Institutional Animal Care and Use Committee (IACUC) of Nanjing Medical University.

For subcutaneous tumors, Hepa1-6 cells ($3–4 \times 10^6$) were injected into the flanks in a 100 μL mixture of Matrigel (Corning) and cell suspension. For in vivo treatments, mice were randomized into the indicated groups on days 5 post-implantation. VB2 (50 mg/kg), FMN (50 mg/kg), FAD (50 mg/kg), or control solvent was administered intratumorally daily from days 5 to 21. Hesperidin (100 mg/kg) or

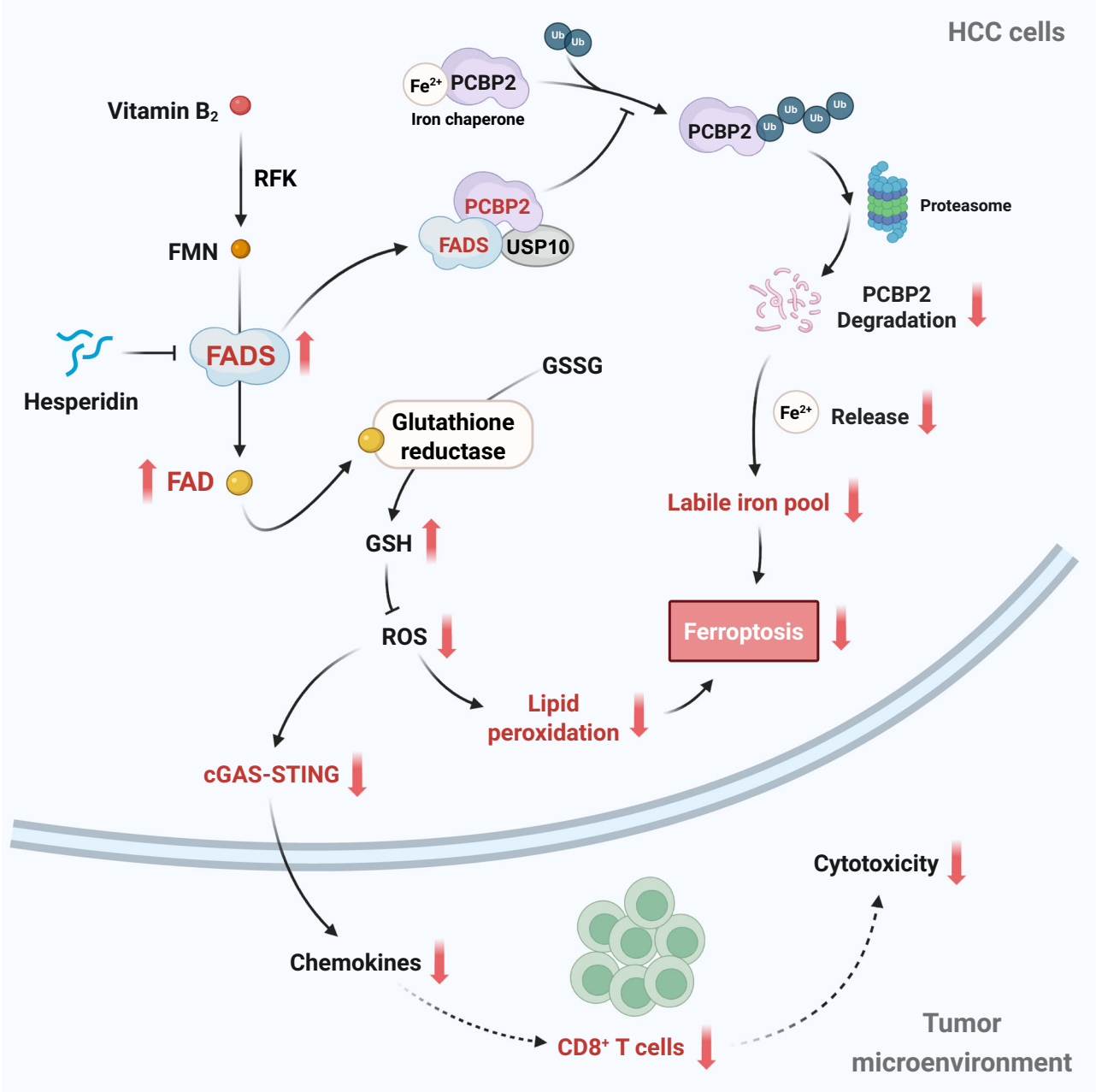

Fig. 8 | Mechanistic insights into the role of VB2 metabolism and FADS in HCC progression (created in BioRender. Chao, J. (2025) https://BioRender.com/oomc25g).

DMSO was administered intraperitoneally daily from days 5 to 21. Tumor size (length × width² × 0.5) was measured bi-weekly, and mice were euthanized on day 21 for tumor harvest. For orthotopic tumors, Hepa1-6 cells or Hepa1-6-lucifese cells ($1–2 \times 10^6$) were injected into the left liver lobe using a 25 µL Matrigel-cell suspension mix. Bioluminescence imaging was performed on days 14 and 21 using an IVIS 100 system (Xenogen). Mice were euthanized on day 21 for further analysis. The method for euthanasia involves initial anesthesia with isoflurane followed by carbon dioxide inhalation. The maximal tumor burden permitted by the IACUC of Nanjing Medical University is 10% weight of the chosen animal, and the maximal tumor burden in our experiments was not exceeded.

Cell culture

HCCLM3 and Hep3B (human HCC cell), Hepa1-6 (mouse HCC cell), and 293T (human embryonic kidney cell) were obtained from the Cell Bank of Type Culture Collection of the Chinese Academy of Sciences (Shanghai, China). The human normal hepatocyte cell line THLE-2 was purchased from Pricella Biotechnology Co., Ltd. (Wuhan, China). All cell lines were cultured in DMEM supplemented with 10% fetal bovine serum and 1% penicillin-streptomycin. For THLE-2 cells, the medium was additionally supplemented with 5 ng/mL human epidermal growth factor (hEGF) and 70 ng/mL phosphoethanolamine. Ham's F-12 medium was used in experiments requiring VB2, FMN, or FAD supplementation due to its low VB2 concentration (0.037 mg/L). All cell lines were authenticated via short tandem repeat profiling and confirmed to be free of mycoplasma contamination.

Cell transfection

The shRNA targeting *RFK* (human), *FLAD1* (human), and *Flad1* (mouse) were generated. The sequences are as follows: sh*RFK*, 5′-GCATACCTTCAAAGAGGACTT-3′; sh*FLAD1*, 5′-GGCTGGCATCATCATTGTTGG-3′; sh*Flad1*, 5′-GTGACAGCAGGCATCATCA-3′. Knockdown of target gene expression was achieved by lentiviral-

mediated shRNA transfection. Overexpression of *Pcbp2* (mouse) were achieved by a lentiviral vector expressing the coding sequence. Stable cell lines were selected using puromycin selection. For transient overexpression, plasmids encoding RFK, FLAD1, PCBP2, 3xFlag-FLAD1, 6xHis-PCBP2, and HA-ubiquitin were transfected into cells using Lipofectamine 3000 (Invitrogen). All plasmids and vectors were obtained from Genechem Co., Ltd. (Shanghai, China).

Chemicals
VB2 (MCE, #HY-B0456), FMN (MCE, #HY-B0964), FAD (MCE, #HY-B1654), Lumiflavin (MCE, #HY-121608), H-151 (MCE, #HY-112693), Robinin (TargetMol, #T2S0265), Rutin hydrate (TargetMol, #T22417), Steviolbioside (TargetMol, #T4964), Linarin (TargetMol, #T6S0653), Hesperidin (TargetMol, #T1035).

qRT-PCR
Total RNA was isolated using a total RNA isolation kit (Vazyme) and reverse transcribed with HiScript RT SuperMix for qPCR (Vazyme). qPCR was performed using SYBR Green PCR Master Mix (Vazyme) on an Applied Biosystems QuantStudio 3 system (Thermo Fisher Scientific). Expression levels were normalized to β-actin, and primer sequences are listed in Supplementary Data. 6.

Western blotting
Proteins were extracted with RIPA buffer, separated by SDS–PAGE, and transferred to PVDF membranes. After blocking, membranes were incubated overnight at 4 °C with primary antibodies. Antibody information: β-actin (CST, #4970, 1:1000), RFK (Santa Cruz, #sc-398830, 1:500), FADS (Proteintech, #68491-1-Ig, 1:5000), PCBP2 (ABclonal, #A23987, 1:2000), FLAG-tag (ABclonal, #AE005, 1:10000), His-tag (ABclonal, #AE003, 1:5000), HA-tag (ABclonal, #AE008, 1:2000), USP10 (Proteintech, #19374-1-AP, 1:1000), cGAS (Proteintech, #26416-1-AP, 1:2000), STING (Proteintech, #80365-RR, 1:1000), TBK1 (CST, #3504, 1:1000), phospho-TBK1 (CST, #5483, 1:1000), IRF3 (Proteintech, #11312-1, 1:5000), and phospho-IRF3 (CST, #29047, 1:1000). Signals were detected using HRP-conjugated secondary antibodies and ECL reagents.

Immunohistochemistry (IHC) and multiplex IHC (mIHC)
Primary antibodies used for IHC or mIHC included: anti-RFK (Atlas, #HPA057163, 1:200), anti-FADS (Affinity, #DF14820, 1:100), anti-PCBP2 (Abcam, #ab184962, 1:100), and anti-CD8α (Abcam, #ab245118, 1:250). IHC results were evaluated by H-score, a semiquantitative approach. Staining intensity was classified as negative (−), weak (+), moderate (++), or strong (+++). The H-score was calculated using the formula: 1 × (% weak staining cells) + 2 × (% moderate staining cells) + 3 × (% strong staining cells). The density of $CD8^+$ T cells was quantified as the number of strongly stained cells per field using ImageJ software. For mIHC, three consecutive paraffin sections were deparaffinized in xylene and rehydrated in ethanol. Heat-induced antigen retrieval was performed in EDTA buffer (pH 9.0). Sections were blocked for 10 min and incubated sequentially with primary antibodies, HRP-conjugated secondary antibodies, and tyramide signal amplification (TSA). After each TSA round, antigen retrieval and antibody stripping were performed. Nuclei were counterstained with DAPI. Images were acquired using a Thunder Imaging System (Leica) and analyzed with SlideViewer software (3DHISTECH).

Immunoprecipitation and mass spectrometry (IP-MS)
Cells were lysed in NP-40 buffer. Protein A/G magnetic beads (Selleck) were first incubated with primary antibodies for 1 h, then incubated with cell lysates overnight at 4 °C. Beads were washed, resuspended in SDS loading buffer, and heated at 100 °C for 5 min. Antibodies used for IP included anti-FADS (Santa Cruz, #sc-376819, 1:40), anti-PCBP2 (ABclonal, #A23987, 1:100), anti-FLAG-Tag (ABclonal, #AE005, 1:200), and anti-His-Tag (ABclonal, #AE003, 1:200). Immunoprecipitates were analyzed by Western blotting or by liquid chromatography-mass spectrometry (Easy-nLC 1000-Q Exactive, Thermo Fisher Scientific). Candidate FADS-interacting proteins identified by IP-MS are listed in Supplementary Data. 5.

Immunofluorescence (IF)
Cells were fixed with 4% paraformaldehyde, permeabilized with 0.2% Triton X-100, and then blocked. Cells were incubated overnight at 4 °C with primary antibodies, including: anti-FADS (Santa Cruz, #sc-376819, 1:50), anti-PCBP2 (Abcam, #ab184962, 1:250), and anti-γ-H2AX (ABclonal, #AP0687, 1:1000). Following this, cells were incubated with Alexa Fluor 488 or Alexa Fluor 594 conjugated secondary antibodies for 1 h and stained with DAPI for nuclear visualization. Quant-iT PicoGreen dsDNA Reagent (Invitrogen, #P7581, 1:500) was used to detect double-stranded DNA (dsDNA), with cells incubated with diluted working solution for 10 min. Images were captured using a confocal microscope (Olympus).

Untargeted metabolomics
Cells were collected and resuspended in pre-chilled 80% methanol, followed by vortexing, sonication, and centrifugation. The supernatant was freeze-dried and reconstituted in 10% methanol for ultra-high-performance liquid chromatography-mass spectrometry (UHPLC-MS/MS) analysis using a Vanquish UHPLC system coupled with an Orbitrap Q Exactive™ HF mass spectrometer (ThermoFisher). Data processing, including peak alignment, detection, and quantification, was performed using Compound Discoverer 3.3 (ThermoFisher). Metabolite annotation utilized the KEGG database, with differentially expressed metabolites defined by VIP >1, $P < 0.05$, and fold change >1.5 or <0.667 (Supplementary Data. 4). Pathway enrichment analysis considered $P < 0.05$ as significant. The analysis was conducted in collaboration with Novogene Co., Ltd. (Beijing, China).

Measurement of flavin adenine dinucleotide (FAD)
FAD levels were quantified using the FAD Assay Kit (Abcam, #ab204710) following the manufacturer's protocol. FAD functions as a cofactor for an oxidase, generating a product that reacts with the OxiRed probe to produce a measurable signal. Optical density was recorded at 570 nm. A Deproteinizing Sample Preparation Kit (AAT Bioquest, #19501) was used to extract FAD from proteins before measurement.

Cell Counting Kit-8 (CCK-8) and colony formation assays
For the CCK-8 assay, cells were seeded in 96-well plates, and at the indicated timepoints, CCK-8 solution (Beyotime) was added to replace the culture medium. After incubation at 37 °C for 2 h, absorbance at 450 nm was measured using a microplate reader. For the colony formation assay, cells were plated in 6-well plates and cultured for 14 days, then fixed and stained with crystal violet (Beyotime).

Migration and invasion assays
Cell migration and invasion were evaluated using 24-well transwell chambers (Corning), but for the invasion assay, the upper chamber was pre-coated with Matrigel. Cells in serum-free medium (200 μL) were seeded in the upper chamber, while the lower chamber contained medium with 10% FBS. After 24 h, migrated cells were fixed in paraformaldehyde and stained with crystal violet, and photos were taken.

ROS, lipid peroxidation and labile iron pool
For ROS and labile iron pool measurements, cells were trypsinized and incubated in serum-free medium at 37 °C for 30 min with 5 μM dihydroethidium (DHE; MCE, #HY-D0079) for ROS and 1 μM FerroOrange (Dojindo, #F374) for labile iron, followed by analysis on a flow cytometer (BD Biosciences) or a SpectraMax iD3 microplate reader

(Molecular Devices). Lipid peroxidation was measured by BODIPY 581/591 C11 staining and malondialdehyde (MDA) quantification. Cells were trypsinized and incubated with 10 μM BODIPY 581/591 C11 (Invitrogen, #D3861) for 30 min at 37 °C, followed by analysis on a flow cytometer (BD Biosciences). MDA levels were measured using the MDA Colorimetric Assay Kit (Elabscience, #E-BC-K028) according to the manufacturer's instructions.

GSH, GSH/GSSG ratio, and glutathione reductase (GR) activity

Cells were lysed, and supernatants were collected. GSH and GR activity were assessed using respective Colorimetric Assay Kits (Elabscience, #E-BC-K097 & #E-BC-K099), according to the manufacturer's protocols.

Cell death measurement

Cells were treated, collected, and then resuspended in PBS containing 1 μg/ml 7-AAD for 5 min, and directly run on a flow cytometer.

Flow cytometry for intratumoral $CD8^+$ T cells

Tumors were excised and cut into approximately 1 mm^3 pieces in RPMI-1640 medium. Tissues were enzymatically digested with Collagenase (1 mg/ml, Sigma-Aldrich) and DNase I (0.1 mg/ml, Sigma-Aldrich) for 30 min at 37 °C with shaking. Cell suspensions were filtered through a 70 μm cell strainer and centrifuged at 400 × *g* for 5 min at 4 °C. After removing the supernatant, pellets were resuspended in red blood cell lysis buffer and incubated for 3 min at room temperature, followed by two PBS washes. Cells were then resuspended in FACS buffer, and lymphocytes were enriched using a lymphocyte separation medium. For identifying $PD\text{-}1^+$ $CD8^+$ T cells, cells were stained with LIVE/DEAD Fixable Viability Dye (eBioscience), Brilliant Violet 650 anti-mouse CD8α (BioLegend, #100741, 1:200) and PE anti-mouse CD279 (PD-1) (BioLegend, #114117, 1:200). For identifying $IFNγ^+$ $CD8^+$ T cells, cells were stimulated with Cell Activation Cocktail (BioLegend, #423303) in culture medium at 37 °C for 4 h before surface staining, then fixed and permeabilized with Fix/Perm solution (BD Biosciences) at 4 °C for 1 h. After washing with Perm/Wash solution (BD Biosciences), cells were stained with PE/Cy7 anti-mouse IFNγ (BioLegend, #505826, 1:200). Data were acquired using FACSCelesta Flow Cytometer (BD Biosciences) and analyzed with FlowJo software. Gating strategies were shown in Supplementary Fig. 11.

Bulk RNA-Seq for HCC cells

Total RNA was extracted, and cDNA libraries were constructed using U-mRNAseq Library Prep Kit (KAITAI-BIO, #AT4221) with Ribo-off rRNA Depletion Kit (Vazyme, #N407). Sequencing was performed on the Illumina NovaSeq X Plus PE150 platform by Hangzhou Kaitai Biotechnology Co., Ltd. (Hangzhou, China). Sequenced reads were aligned to the human reference genome using HISAT2, and binary alignment map (BAM) files were generated. Gene expression was quantified as fragments per kilobase of transcript per million mapped reads (FPKM) using StringTie with default parameters. Differentially expressed genes (DEGs) were identified using edgeR with criteria of fold change >2 or <0.5, P-value < 0.05, and FDR <0.05. Enriched pathways were identified using the fgsea package for Gene Set Enrichment Analysis (GSEA). Raw data are publicly accessible in the Genome Sequence Archive (GSA-Human: HRA008980).

Single-Cell RNA-Seq for human HCC tumors

Biopsy samples from the Immunotherapy Cohort were processed using a Multi-tissue Dissociation Kit, and scRNA-seq libraries were prepared with the SeekOne MM Single Cell 3' Library Kit. Sequencing was conducted on an Illumina NovaSeq 6000 (PE150). Read mapping and UMI generation were performed using SeekOne Tools with the GRCH38 genome as a reference. Data analysis followed the Seurat pipeline, incorporating Harmony for batch effect correction. Dimensionality reduction and clustering were conducted using t-SNE, with detailed methods as described in a previous report[40]. Raw data are publicly accessible in the Genome Sequence Archive (GSA-Human: HRA012300).

Single-Cell RNA-Seq for mouse tumors

Orthotopic tumors generated using Hepa1-6 cells (Control and shFlad1) were harvested on day 14 post-implantation. Single-cell suspensions were prepared, and sequencing libraries were constructed using the DNBelab C-TaiM4 system. Sequencing was performed on the DNBSEQ-T7RS platform by Hangzhou Kaitai Biotechnology Co., Ltd. (Hangzhou, China). The Seurat package (v4.1.1) was applied for downstream analysis. Cells with less than 1000 UMIs or >15% mitochondria genes were excluded. Harmony was used to remove batch effects. We scaled data with the top 4000 most variable genes by using the FindVariableFeatures function and used variable genes for principal component analysis (PCA), used FindNeighbors to get nearest neighbors for graph clustering based on the top 50 PCs, and used FindCluster to obtain cell subtypes, and visualized cells with the uniform manifold approximation and projection (UMAP) algorithm. Then, the clusters were scored for the previously described gene signatures. We used the "FindAllMarkers" function to identify genes that are differentially expressed between clusters. The wilcoxon's rank-sum test with the Benjamini-Hochberg method was used to obtain p-values and the adjusted p-values for comparisons. Raw data are publicly accessible in the Genome Sequence Archive (GSA: CRA026545).

Gene signatures and scoring

Details of all gene signatures are provided in Supplementary Data. 3. The VB2 metabolism gene signature consists of seven genes (*SLC52A1, SLC52A2, SLC52A3, RFK, FLAD1, ACP5*, and *ENPP1*) based on the Reactome pathway database (https://reactome.org/content/detail/R-HSA-196843). The CD8T signature included twelve genes (*CD3D, CD3E, CD3G, CD8A, CD8B, GZMB, GZMA, NKG7, GZMK, PRF1, CD44*, and *CD69*) as previously described[41]. For canonical T cell classification, we referenced the work of Massimo Andreatta et al.[18] The normal hepatocyte signature included 37 genes selected from the Liver Single Cell Atlas database[17]. The interferon (IFN) signature included 70 genes from Peter Szabo et al.[42] The dysfunction signature included 27 genes from Hanjie Li et al.[43] The proliferation signature included 67 genes from Peter Szabo et al.[42].

For bulk RNA-seq data, we used the ssGSEA algorithm (the gsva function from the GSVA package v1.44.2) to integrate gene signatures and calculate the signature score for each sample. For single-cell RNA-seq data, we used the AUCell algorithm (the RunAUCell function from the pochi package v0.1.0) to integrate the gene signature and compute the signature score for each cell. Comparisons of signature score enrichment between groups were assessed using the two-sided Wilcoxon rank-sum test, with Benjamini-Hochberg correction applied for multiple testing.

Survival analysis

Patients were classified into high and low expression groups based on the optimal cutoff value that maximally separated populations according to survival outcomes. The optimal cutoff was determined using the surv_cutpoint function from the survminer package (v0.4.9). Kaplan-Meier survival analysis was subsequently performed using the survival package in R, and statistical comparisons between groups were made using the log-rank test.

Function enrichment

KEGG enrichment, GO enrichment, and GSEA analysis were implemented in the clusterProfiler R package (v4.7.1.2). Enriched pathways with adjusted $P < 0.05$ were considered as significantly.

Identification of perturbed cell types using the scDist

We used scDist (v1.1.2) to infer the perturbed cell types. The DistPlot function was performed to show the result using default parameters.

High-throughput virtual screening for FADS-targeting compounds

A small molecule library containing approximately 1.6 million compounds was provided by ChemDiv (California, USA). The protonation state of all compounds was set to pH 7.4, and 3D structures were generated using Open Babel. The structure of FADS was generated by AlphaFold. AutoDockTools prepared the receptor protein and compounds. Docking grid files were created using AutoGrid, with the active site pocket identified for small molecule screening. Quick Vina 2 was used for the initial virtual screening, selecting the top 3% of scores for a second round of screening with smina. In the third round, compounds were further analyzed for medicinal properties using QED, selecting those with QED >0.5 while eliminating PAINS constructs to reduce false positives.

Molecular docking

The interaction sites between FADS and PCBP2 were analyzed using molecular docking techniques. The FADS structure was predicted using AlphaFold, while the X-ray crystal structure of the PCBP2 KH1 domain (PDB: 2AXY) was obtained from the Protein Data Bank. Protein preparation was performed with AutoDockTools, and docking simulations were conducted via the ZDock server. The resulting interaction models were visualized using PyMOL. In addition, interactions involving FADS, PCBP2, and USP10 were examined using the same methodology.

To investigate the binding sites of Hesperidin on FADS, the Hesperidin structure was sourced from PubChem, and the FADS structure was generated by AlphaFold. The protonation state of Hesperidin was adjusted to pH 7.4, and its 3D structure was prepared using Open Babel. Protein and compound preparation was conducted using AutoDockTools, followed by docking simulations with AutoDock Vina. The optimal docking pose was analyzed and visualized in PyMOL.

Statistical analysis

Statistical analysis was performed using GraphPad Prism 8 (GraphPad Software, San Diego, CA). Data are presented as mean ± SD or median with interquartile ranges unless otherwise specified. Statistical differences between two groups were assessed using Student's *t* test or the Wilcoxon rank test, as appropriate. Statistical differences of three or more groups were analyzed using ANOVA analysis. $P < 0.05$ were considered significant.

Reporting summary

Further information on research design is available in the Nature Portfolio Reporting Summary linked to this article.

Data availability

The RNA-seq data generated in this study have been deposited in the Genome Sequence Archive (https://ngdc.cncb.ac.cn/) under accession codes HRA008980, HRA012300, and CRA026545. The mass spectrometry proteomics data have been deposited in the ProteomeXchange Consortium (https://proteomecentral.proteomexchange.org) via the iProX partner repository with accession code PXD065100 (https://www.iprox.cn//page/project.html?id=IPX0012310000). The remaining data are available within the Article, Supplementary Information, or Source Data file. Public RNA-seq datasets, including TCGA-LIHC, OEP000321, and ICGC-LIRI-JP, were retrieved from The Cancer Genome Atlas (http://gdac.broadinstitute.org/), the NODE database (https://www.biosino.org/node/), and the International Cancer Genome Consortium (https://icgc.org/), respectively. Data from an anti-PD-1 immunotherapy cohort of 17 HCC patients (Fudan Cohort) were obtained from a published study[15]. Single-cell RNA-seq dataset GSE202642 were sourced from the GEO database (https://www.ncbi.nlm.nih.gov/geo/). The HCCDB database (http://lifeome.net:809/) was used to acquire *RFK* and *FLAD1* expression in 18 HCC datasets. Source data are provided in this paper.

References

1. Vogel, A., Meyer, T., Sapisochin, G., Salem, R. & Saborowski, A. Hepatocellular carcinoma. *Lancet* **400**, 1345–1362 (2022).
2. Xiao, Y. et al. Emerging therapies in cancer metabolism. *Cell Metab.* **35**, 1283–1303 (2023).
3. Kreuzaler, P. et al. Vitamin B(5) supports MYC oncogenic metabolism and tumor progression in breast cancer. *Nat. Metab.* **5**, 1870–1886 (2023).
4. Yang, Y. et al. Dietary vitamin B3 supplementation induces the antitumor immunity against liver cancer via biased GPR109A signaling in myeloid cell. *Cell Rep. Med.* **5**, 101718 (2024).
5. Yuan, X. et al. Vitamin E enhances cancer immunotherapy by reinvigorating dendritic cells via targeting checkpoint SHP1. *Cancer Discov.* **12**, 1742–1759 (2022).
6. Balasubramaniam, S., Christodoulou, J. & Rahman, S. Disorders of riboflavin metabolism. *J. Inherit. Metab. Dis.* **42**, 608–619 (2019).
7. Barile, M., Giancaspero, T. A., Leone, P., Galluccio, M. & Indiveri, C. Riboflavin transport and metabolism in humans. *J. Inherit. Metab. Dis.* **39**, 545–557 (2016).
8. Lienhart, W. D., Gudipati, V. & Macheroux, P. The human flavoproteome. *Arch. Biochem. Biophys.* **535**, 150–162 (2013).
9. Nisco, A., Tolomeo, M., Scalise, M., Zanier, K. & Barile, M. Exploring the impact of flavin homeostasis on cancer cell metabolism. *Biochim. Biophys. Acta Rev. Cancer* **1879**, 189149 (2024).
10. Hu, P. et al. FLAD1 is up-regulated in Gastric Cancer and is a potential prediction of prognosis. *Int. J. Med. Sci.* **17**, 1763–1772 (2020).
11. Nisco, A. et al. Increased demand for FAD synthesis in differentiated and stem pancreatic cancer cells is accomplished by modulating FLAD1 gene expression: the inhibitory effect of Chicago Sky Blue. *Febs J.* **290**, 4679–4694 (2023).
12. Lin, C. C. & Yin, M. C. B vitamins deficiency and decreased antioxidative state in patients with liver cancer. *Eur. J. Nutr.* **46**, 293–299 (2007).
13. Rao, P. N. et al. Elevation of serum riboflavin carrier protein in hepatocellular carcinoma. *Hepatol. Res.* **35**, 83–87 (2006).
14. Zhu, G. Q. et al. CD36(+) cancer-associated fibroblasts provide immunosuppressive microenvironment for hepatocellular carcinoma via secretion of macrophage migration inhibitory factor. *Cell Discov.* **9**, 25 (2023).
15. Wei, C. Y. et al. PKCα/ZFP64/CSF1 axis resets the tumor microenvironment and fuels anti-PD1 resistance in hepatocellular carcinoma. *J. Hepatol.* **77**, 163–176 (2022).
16. Hamilton, P. T., Anholt, B. R. & Nelson, B. H. Tumour immunotherapy: lessons from predator-prey theory. *Nat. Rev. Immunol.* **22**, 765–775 (2022).
17. Brancale, J. & Vilarinho, S. A single cell gene expression atlas of 28 human livers. *J. Hepatol.* **75**, 219–220 (2021).
18. Andreatta, M. et al. Interpretation of T cell states from single-cell transcriptomics data using reference atlases. *Nat. Commun.* **12**, 2965 (2021).
19. Barsch, M. et al. T-cell exhaustion and residency dynamics inform clinical outcomes in hepatocellular carcinoma. *J. Hepatol.* **77**, 397–409 (2022).
20. Kwon, J. & Bakhoum, S. F. The cytosolic DNA-sensing cGAS-STING pathway in cancer. *Cancer Discov.* **10**, 26–39 (2020).
21. Chen, T. et al. NSUN2 is a glucose sensor suppressing cGAS/STING to maintain tumorigenesis and immunotherapy resistance. *Cell Metab.* **35**, 1782–1798.e1788 (2023).

22. Ka, N. L. et al. NR1D1 Stimulates antitumor immune responses in breast cancer by activating cGAS-STING signaling. *Cancer Res.* **83**, 3045–3058 (2023).
23. Srinivas, U. S., Tan, B. W. Q., Vellayappan, B. A. & Jeyasekharan, A. D. ROS and the DNA damage response in cancer. *Redox Biol.* **25**, 101084 (2019).
24. Olfat, N., Ashoori, M. & Saedisomeolia, A. Riboflavin is an antioxidant: a review update. *Br. J. Nutr.* **128**, 1887–1895 (2022).
25. Stockwell, B. R. Ferroptosis turns 10: Emerging mechanisms, physiological functions, and therapeutic applications. *Cell* **185**, 2401–2421 (2022).
26. Yanatori, I., Yasui, Y., Tabuchi, M. & Kishi, F. Chaperone protein involved in transmembrane transport of iron. *Biochem. J.* **462**, 25–37 (2014).
27. Yanatori, I., Richardson, D. R., Imada, K. & Kishi, F. Iron export through the transporter ferroportin 1 is modulated by the iron chaperone PCBP2. *J. Biol. Chem.* **291**, 17303–17318 (2016).
28. Yue, L., Luo, Y., Jiang, L., Sekido, Y. & Toyokuni, S. PCBP2 knockdown promotes ferroptosis in malignant mesothelioma. *Pathol. Int.* **72**, 242–251 (2022).
29. Ferreira de Oliveira, J. M. P., Santos, C. & Fernandes, E. Therapeutic potential of hesperidin and its aglycone hesperetin: Cell cycle regulation and apoptosis induction in cancer models. *Phytomedicine* **73**, 152887 (2020).
30. Roohbakhsh, A., Parhiz, H., Soltani, F., Rezaee, R. & Iranshahi, M. Molecular mechanisms behind the biological effects of hesperidin and hesperetin for the prevention of cancer and cardiovascular diseases. *Life Sci.* **124**, 64–74 (2015).
31. Sheikh, P., Lohsiriwat, V. & Shelygin, Y. Micronized purified flavonoid fraction in hemorrhoid disease: A systematic review and meta-analysis. *Adv. Ther.* **37**, 2792–2812 (2020).
32. Li, K. X., Diendéré, G., Galanaud, J. P., Mahjoub, N. & Kahn, S. R. Micronized purified flavonoid fraction for the treatment of chronic venous insufficiency, with a focus on postthrombotic syndrome: A narrative review. *Res Pr. Thromb. Haemost.* **5**, e12527 (2021).
33. de Vogel, S. et al. Dietary folate, methionine, riboflavin, and vitamin B-6 and risk of sporadic colorectal cancer. *J. Nutr.* **138**, 2372–2378 (2008).
34. Paragomi, P. et al. The association between serum riboflavin and flavin mononucleotide with pancreatic cancer: Findings from a prospective cohort study. *Pancreas* **52**, e127–e134 (2023).
35. Shan, X. et al. Riboflavin kinase binds and activates inducible nitric oxide synthase to reprogram macrophage polarization. *Redox Biol.* **78**, 103413 (2024).
36. Schramm, M. et al. Riboflavin (vitamin B2) deficiency impairs NADPH oxidase 2 (Nox2) priming and defense against Listeria monocytogenes. *Eur. J. Immunol.* **44**, 728–741 (2014).
37. Yuan, C., Chen, M. & Cai, X. Advances in poly(rC)-binding protein 2: Structure, molecular function, and roles in cancer. *Biomed. Pharmacother.* **139**, 111719 (2021).
38. Shen, L. et al. PHGDH Inhibits ferroptosis and promotes malignant progression by upregulating SLC7A11 in bladder cancer. *Int. J. Biol. Sci.* **18**, 5459–5474 (2022).
39. Aggarwal, V. et al. Molecular mechanisms of action of hesperidin in cancer: Recent trends and advancements. *Exp. Biol. Med.* **245**, 486–497 (2020).
40. Li, Y. et al. Immunosuppression and phenotypic plasticity in an atlas of human hepatocholangiocarcinoma. *Hepatobiliary Surg. Nutr.* **13**, 586–603 (2024).
41. Wang, H. et al. POSTN(+) cancer-associated fibroblasts determine the efficacy of immunotherapy in hepatocellular carcinoma. *J. Immunother. Cancer* **12**, https://doi.org/10.1136/jitc-2023-008721 (2024).
42. Szabo, P. A. et al. Single-cell transcriptomics of human T cells reveals tissue and activation signatures in health and disease. *Nat. Commun.* **10**, 4706 (2019).
43. Li, H. et al. Dysfunctional CD8 T cells form a proliferative, dynamically regulated compartment within human melanoma. *Cell* **181**, 747 (2020).

Acknowledgements

This work was supported by the CAMS Innovation Fund for Medical Sciences (2019- I2M-5-035, to L.L.), the National High-Level Hospital Clinical Research Funding (2022-PUMCH-B-128, to H.Z.), and the Fundamental Research Funds for the Central Universities (3332024129, to Z.Y.X.).

Author contributions

L.L., H.Z., and F.C. designed and supervised the study. J.C., Y.L., H.W., Z.Y.X., S.W., and Z.F.X. conducted experiments and analyzed the data. M.W., Q.H., R.Z., M.L., L.Z., B.S., and Y.Z. provided study materials and technical support. J.C. and Y.L. drafted the manuscript. All the authors read and approved the manuscript.

Competing interests

The authors declare no competing interests.

Additional information

Supplementary information The online version contains supplementary material available at https://doi.org/10.1038/s41467-025-64572-y.

Correspondence and requests for materials should be addressed to Feng Cheng, Haitao Zhao or Ling Lu.

Peer review information *Nature Communications* thanks Jan Grimm and the other anonymous reviewer(s) for their contribution to the peer review of this work. A peer review file is available.